

Article

Revolutionizing Battery Longevity by Optimising Magnesium Alloy Anodes Performance

Bankole I. Oladapo ^{1,*}, **Matthew A. Olawumi** ² and **Francis T. Omigbodun** ³ ¹ School of Science and Engineering, University of Dundee, Dundee DD1 4HN, UK² Computing, Engineering and Media, De Montfort University, Leicester LE1 9BH, UK; olawumisola13@gmail.com³ Wolfson School of Mechanical, Electrical and Manufacturing Engineering, Loughborough University, Loughborough LE11 3TU, UK; f.omigbodun@lboro.ac.uk

* Correspondence: p17243433@my365.dmu.ac.uk

Abstract: This research explores the enhancement of electrochemical performance in magnesium batteries by optimising magnesium alloy anodes, explicitly focusing on Mg-Al and Mg-Ag alloys. The study's objective was to determine the impact of alloy composition on anode voltage stability and overall battery efficiency, particularly under extended cycling conditions. The research assessed the anodes' voltage behaviour and internal resistance across magnesium bis(trifluoromethanesulfonyl)imide ($Mg(TFSI)_2$) electrolyte formulations using a systematic setup involving cyclic voltammetry on the anode and electrochemical impedance spectroscopy. The Mg-Al alloy demonstrated superior performance, with minimal voltage drop and lower resistance increase than the Mg-Ag alloy. The results showed that the Mg-Al alloy maintained over 85% energy efficiency after 100 cycles, significantly outperforming the Mg-Ag alloy, which exhibited increased degradation and efficiency reduction to approximately 80%. These findings confirm that incorporating aluminium into magnesium anodes stabilises the anode voltage and enhances the overall battery efficiency by mitigating degradation mechanisms. Consequently, the Mg-Al alloy is identified as an up-and-coming candidate for use in advanced battery technologies, offering energy density and cycle life improvements. This study lays the groundwork for future research to refine magnesium alloy compositions further to boost battery performance.



Citation: Oladapo, B.I.; Olawumi, M.A.; Omigbodun, F.T.. Revolutionizing Battery Longevity by Optimising Magnesium Alloy Anodes Performance. *Batteries* **2024**, *10*, 383. <https://doi.org/10.3390/batteries10110383>

Academic Editors: Xiaoyuan Shi, Hengguo Wang and Hirotoshi Yamada

Received: 14 September 2024

Revised: 16 October 2024

Accepted: 28 October 2024

Published: 30 October 2024



Copyright: © 2024 by the authors. Licensee MDPI, Basel, Switzerland. This article is an open access article distributed under the terms and conditions of the Creative Commons Attribution (CC BY) license (<https://creativecommons.org/licenses/by/4.0/>).

1. Introduction

Magnesium batteries, known for their high energy density and safety due to the use of magnesium metal, represent a promising alternative to traditional lithium-ion technologies. Magnesium offers a theoretical volumetric capacity of 3833 mAh/cm^3 as a divalent cation, significantly higher than lithium's (2061 mAh/cm^3) [1–3]. This attribute and magnesium's earth-abundance and inherent safety underscore its potential in developing next-generation battery systems.

The anode voltage is critical for magnesium batteries' energy density and efficiency. A lower anode potential relative to the magnesium ion/metal couple is desirable as it increases the voltage window of the cell, thereby enhancing the battery's specific energy [4–6]. However, achieving a stable and high-performance anode with a low and effective voltage has proven to be a complex challenge due to the intrinsic electrochemical properties of magnesium and its interaction with common electrolytes [7–9].

The exploration of magnesium as a battery material began in the early 2000s, focusing initially on overcoming the challenges posed by Mg's high ionisation tendency and difficulty finding compatible electrolytes. Early studies dealt primarily with salt-based

electrolytes, which facilitated some ionic movement but were hindered by rapid degradation and passivation at the anode surface [10–12]. Extensive research has explored various anode materials, from elemental magnesium to alloys and intermetallic compounds. These studies have identified critical performance factors, such as anode–electrolyte interface stability and ion transport mechanisms. Recent advancements have introduced novel anode materials showing reduced passivation and compatibility with high-performance electrolytes [13–15].

Despite significant advancements, several critical gaps remain in the literature and practical application. Most magnesium anodes still suffer from issues related to long-term cycling stability, which is often compromised by the formation of insulating films on the anode surface [16–18]. The interaction between the anode and electrolyte remains imperfect, with many current electrolyte formulations either chemically degrading the anode material or offering insufficient ionic conductivity. While anodes have shown promising lab-scale results, translating these findings to commercially viable solutions is often unaddressed. The cost implications of novel materials and electrolytes have not been sufficiently explored [19–21].

This study addresses these gaps by proposing a systematic investigation into novel magnesium alloys as anodes, examining their electrochemical performance across complex electrolytes. The research will exclude traditional pure magnesium anodes and focus instead on those incorporating elements like aluminium and silicon, which preliminary studies suggest may offer enhanced performance [22–24]. The literature review encompasses many sources, from seminal papers introducing magnesium as a viable battery material to recent publications that detail advancements in anode technology and $(\text{Mg}(\text{TFSI})_2)$ electrolyte development. Each selected work has been evaluated for its relevance to the ongoing challenges in the field, ensuring a comprehensive overview of past achievements and current shortcomings [25–27]. The present research intends to fill the identified gaps by developing anode materials that sustain high electrochemical performance without the typical degradation in current magnesium batteries. By doing so, it hopes to pave the way for the next generation of high-energy, safe, and cost-effective storage solutions [28–30].

Magnesium batteries offer a theoretical volumetric capacity of 3833 mAh/cm³, higher than lithium-ion batteries, alongside other benefits like safety and cost-effectiveness. However, magnesium anodes face significant challenges, such as passivation and compatibility with electrolytes, which affect long-term cycling stability [30–32]. This research addresses these issues by evaluating Mg-Al and Mg-Ag alloy anodes, focusing on voltage stability, cycling efficiency, and internal resistance.

Magnesium batteries have attracted considerable attention as a viable substitute for conventional lithium-ion technology, chiefly because of their superior theoretical volumetric capacity, intrinsic safety, and the plentiful availability of magnesium. Nonetheless, despite these benefits, the extensive implementation of magnesium batteries has been obstructed by several significant problems, especially regarding the efficacy of magnesium anodes. Confronting these problems is essential for enhancing magnesium batteries' overall effectiveness and stability, rendering them suitable for commercial and high-demand applications [32,33].

A significant concern of magnesium anodes is their long-term cycling stability. Magnesium anodes exhibit degradation during successive charge–discharge cycles, resulting in a substantial decline in battery capacity and efficiency. The degradation is frequently intensified by the development of passivation layers on the anode surface, obstructing the passage of magnesium ions, hence diminishing overall conductivity and battery longevity. Anode passivation constitutes a significant impediment to the efficient utilization of magnesium in batteries, as it adversely affects performance during cycling and elevates internal resistance, thus diminishing energy production [34,35].

Moreover, $(\text{Mg}(\text{TFSI})_2)$ electrolyte compatibility presents a significant obstacle for magnesium batteries. Numerous traditional electrolytes employed in lithium-ion batteries exhibit incompatibility with magnesium since they either chemically deteriorate the mag-

nesium anode or inadequately promote effective ion transport. The interaction between the electrolyte and the magnesium anode frequently generates unwanted by-products, exacerbating passivation and constraining the battery's efficiency. This requires the creation of novel $(\text{Mg}(\text{TFSI})_2)$ electrolyte formulations that can function synergistically with magnesium anodes, minimizing deterioration while preserving ion transport efficiency [36–38]. This study primarily examines these challenges by exploring the application of Mg-Al and Mg-Ag alloy anodes, to improve voltage stability, minimizing deterioration, and enhance compatibility with diverse $(\text{Mg}(\text{TFSI})_2)$ electrolytes. The project intends to address these critical obstacles to develop high-efficiency, durable magnesium batteries.

This research addresses critical challenges associated with magnesium anodes in magnesium batteries, specifically focusing on improving voltage stability, cycling efficiency, and mitigating degradation mechanisms. Magnesium anodes, while offering advantages like higher theoretical volumetric capacity and safety compared to lithium-ion technologies, face significant obstacles such as long-term cycling stability issues, passivation, and $(\text{Mg}(\text{TFSI})_2)$ electrolyte compatibility. This study aims to explore the electrochemical performance of two magnesium alloy anodes—Mg-Al and Mg-Ag—by investigating their voltage stability and internal resistance over extended cycling. By incorporating aluminium and silicon into magnesium, the research seeks to enhance anode durability, reduce degradation, and optimize the battery's overall performance. The study employs cyclic voltammetry (CV) and electrochemical impedance spectroscopy (EIS) to evaluate the electrochemical properties of the anodes, such as oxidation/reduction potentials and internal resistance. The goal is to identify how these novel alloy compositions interact with various $(\text{Mg}(\text{TFSI})_2)$ electrolyte formulations to mitigate common issues like rapid capacity fade and anode passivation. Ultimately, the research aims to contribute to developing more stable and efficient magnesium-based batteries, offering improved energy density and longer cycle life, which could be viable alternatives to current lithium-ion technologies.

2. Methodology

The study is structured around a series of electrochemical tests to evaluate the performance of novel magnesium alloys as anodes in magnesium batteries. Each computation mimics realistic operational conditions while allowing precise control over temperature, $(\text{Mg}(\text{TFSI})_2)$ electrolyte composition, and current density [31–33].

2.1. Cell and Electrolyte Configuration

The computational cells are assembled using a standard coin cell configuration, including a magnesium alloy anode, a high-purity magnesium reference electrode, and a manganese dioxide cathode. This setup is chosen to ensure compatibility with a wide range of $(\text{Mg}(\text{TFSI})_2)$ electrolytes while minimising the introduction of side reactions. Multiple $(\text{Mg}(\text{TFSI})_2)$ electrolytes, varying primarily in solvent and salt composition, are prepared to explore the interaction effects with the anode material. The $(\text{Mg}(\text{TFSI})_2)$ electrolytes are meticulously prepared under an inert atmosphere to prevent contamination and pre-testing degradation. All tests are conducted in a temperature-controlled environment, maintaining a steady temperature of 25 °C to eliminate the influence of thermal fluctuations on the results.

2.2. Description of the Anode Materials Used

The anode materials selected for this study are primarily magnesium alloys, enhanced with small percentages of aluminium and silicon, which are hypothesised to improve the electrochemical performance and stability of the anodes. Mg-Al Alloy is comprised of 95% magnesium and 5% aluminium. Aluminium is expected to enhance the flexibility and corrosion resistance of the anode. Mg-Ag alloy contains 90% magnesium and 10% silicon, aimed at improving the conductivity and reducing the anode's susceptibility to passivation. Each alloy is synthesised using a melt-spinning process that ensures homogeneity and fine microstructure, critical for consistent electrochemical behaviour [34–36] (Figure 1).

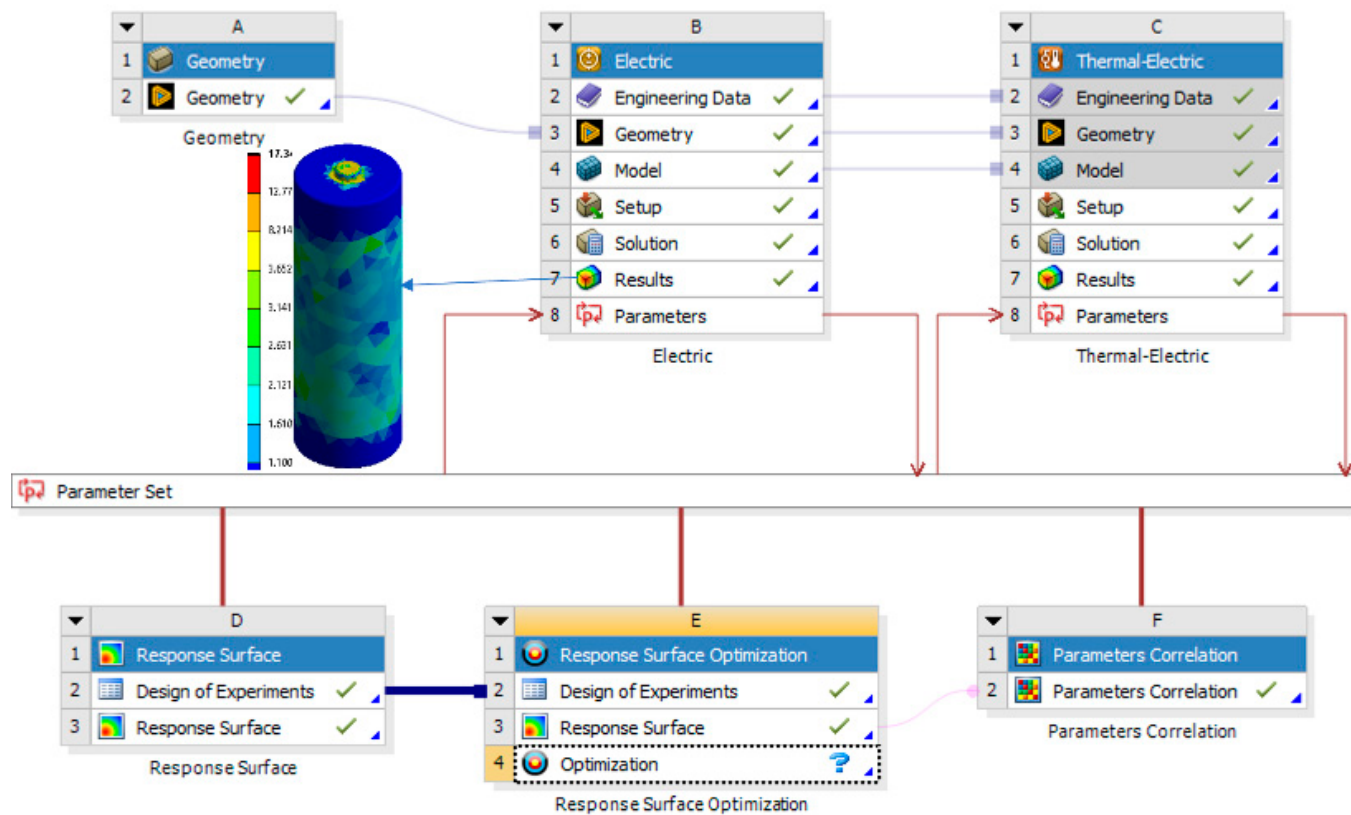


Figure 1. An optimum model design of the magnesium anode.

2.3. Measurement Techniques for Anode Voltage

Anode voltage is measured using a high-precision voltmeter connected to the working electrode and a stable reference electrode. The voltage is recorded continuously throughout the charge–discharge cycles to monitor any potential drops that may indicate degradation or inefficiency. Cyclic voltammetry (CV) characterises the anodes’ electrochemical properties, including their oxidation and reduction potentials. The scan rate is set at 0.1 mV/s to ensure detailed resolution of the electrochemical reactions occurring at the anode surface. Electrochemical impedance spectroscopy (EIS) is utilised to measure the internal resistance of the anodes, which is a critical factor affecting the voltage efficiency [37,38]. Measurements are taken before and after each cycling test to assess any changes in resistance that could indicate degradation. Cyclic voltammetry (CV) and electrochemical impedance spectroscopy (EIS) will measure the alloys’ voltage behaviour and internal resistance. A constant temperature of 25 °C will be maintained during all tests to ensure stable conditions.

2.4. Reproducible Methodology to Identify Relevant Works

The methodology to identify and select the relevant literature involves a structured approach using multiple academic database studies published in the last ten years, involving magnesium or magnesium alloys used in battery anodes reporting primary data on electrochemical tests [39–41]. This systematic approach ensures comprehensive coverage of existing knowledge, while identifying the gaps the current study aims to address. This methodology section outlines a detailed, reproducible framework for conducting high-quality, controlled magnesium alloy anodes and systematically reviewing the literature to inform designs and hypotheses [42–44]. Figure 2 typically develops a series of diagrams or schematics that clearly illustrate the components and configurations used in measuring the voltage of an anode. This would be valuable for educational purposes, training, or ensuring consistency in research settings. Anode voltage measurement setups often involve specific hardware components and configurations, including the anode material, (Mg(TFSI)₂) elec-

trolyte, reference, counter electrodes, and equipment for voltage measurement, and data logging [45–47]. Such a guide represents these setups to facilitate visual understanding and reproducibility.

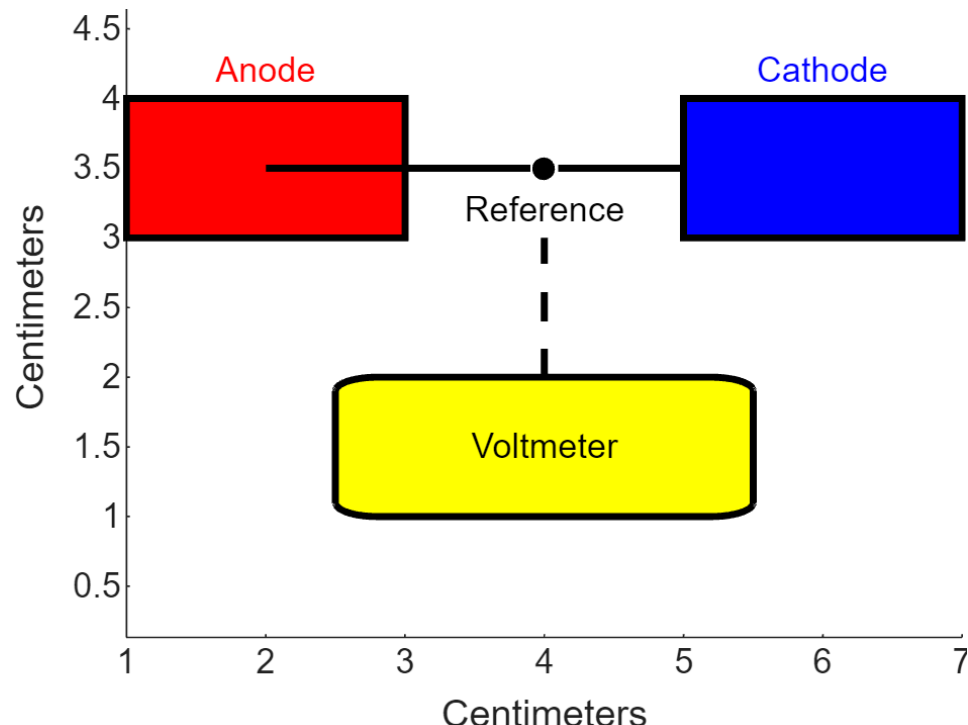


Figure 2. Computation setup for anode voltage measurement: A visual guide.

Identify key components of the list of all critical elements required for the setup. The design layout conceptualises how these components are physically arranged and connected. Generate the visual guide using MATLAB to create diagrams or schematics visually representing the setup. Draw components of rectangle and plot functions are used to draw electrodes and connections. The voltmeter connection is a dashed line showing the voltmeter's connection to the point between the reference and working electrodes [48–50]. This simple visual guide helps users understand the basic setup for measuring anode voltage. The schematic can be more complex by adding $(\text{Mg}(\text{TFSI})_2)$ electrolyte containers, different electrode materials, or more sophisticated measuring equipment.

The $(\text{Mg}(\text{TFSI})_2)$ electrolytes used in this study include combinations of magnesium salts ($\text{Mg}(\text{TFSI})_2$) and solvents such as ethylene carbonate (EC), propylene carbonate (PC), and dimethyl carbonate (DMC). Details of concentrations will be provided in a dedicated table. The anode material composition of Mg-Al alloy: 95% Mg, 5% Al, and Mg-Ag alloy: 90% Mg, 10% Si. These compositions were selected based on their potential to improve the stability and corrosion resistance of the anodes.

3. Mathematical Model

A mathematical equation that encompasses the analysis of anode voltage and overall battery performance in magnesium batteries considers the following key factors. V_{oc} is the open-circuit voltage of the battery, R_i is the internal resistance of the battery, and I is the current through the battery. C is the capacity of the battery, n is the number of charge/discharge cycles, and η is the efficiency of the battery. One essential performance metric in battery analysis is voltage efficiency, which can be calculated by considering the operating voltage under load compared to the open-circuit voltage [51–53]. A derived formula to estimate a magnesium battery's effective operating voltage and efficiency, considering anode degradation over cycles is shown below.

3.1. Effective Operating Voltage

$$V_{eff}(n) = V_{oc} - I \cdot R_i(n)$$

where $R_i(n)$ is the internal resistance, which could increase over the number of cycles n due to material degradation or other factors.

$$\text{Battery efficiency } \eta(n) = ((V_{eff}(n))/V_{oc}) \cdot 100\%$$

Battery capacity fade accounts for capacity degradation over cycles; a standard empirical model that can be used is

$$C(n) = C(1) \cdot e^{-k \cdot n}$$

where $C(1)$ is the initial capacity, k is a constant representing the capacity fade rate, and n is the number of cycles.

3.2. Complete Model for Voltage and Efficiency

Combining these equations, we can create a comprehensive model that provides insights into how the anode material and degradation affect the battery's performance over time. The model could simulate performance under different scenarios and optimise the battery design.

$$V_{total}(n, I) = V_{oc} - I \cdot R_i(n)$$

$$\eta_{(total)}(n, I) = ((V_{(total)}(n, I))/V_{oc}) \cdot (C(n)/C(1)) \cdot 100\%$$

These equations help quantify the impact of anode material changes, usage patterns, and other variables on the performance of magnesium batteries, which is crucial for their development and optimisation for commercial use.

3.3. Extended Model

A more advanced and complex mathematical model for analysing the performance of magnesium battery anodes was modelled. We introduce factors influencing battery behaviour, such as temperature effects, anode–cathode interaction, and $(\text{Mg(TFSI})_2$) electrolyte conductivity. The model will incorporate differential equations to simulate dynamic behaviour during battery operation. Dynamic voltage model incorporates temperature dependence and voltage response to variable load conditions, using a resistance that changes with temperature and current [54–56]. Temperature influence was considered to be the impact of temperature on internal resistance and battery capacity, which affects both performance and degradation rate. Rate of voltage change concerning time for a model of how voltage decreases over time due to internal chemical and physical changes.

3.3.1. Dynamic Voltage Equation

$$\frac{dV}{dt} = -\frac{I(t)}{C} - \frac{V(t) - E_{oc}(T)}{R_i(T, I)}$$

where $V(t)$ is voltage at time t , $I(t)$ is current at time t , and C is battery capacity. $E_{oc}(T)$ is open-circuit voltage dependent on temperature T , and $R_i(T, I)$ is the internal resistance dependent on temperature T and current I .

3.3.2. Temperature-Dependent Internal Resistance

$$R_i(T, I) = R_0 \cdot (1 + \alpha(T - T_{ref})) \cdot (1 + \beta I^2)$$

R_0 is the reference internal resistance at temperature T_{ref} , and α, β are the temperature and current coefficients for resistance change.

3.3.3. Battery Capacity with Temperature and Cycle Number

$$C(T,n) = C_0 \cdot e^{-k(T) \cdot n}$$

where C_0 initial capacity, $k(T)$ is a temperature-dependent rate of capacity fade, and n is the number of cycles.

3.3.4. Numerical Simulation Approach

Time step Δt is the small time interval for simulation (e.g., 1 s). Simulation duration: Total time for simulation (e.g., 3600 s for a 1-h test) and initial conditions $V(0) = E_{oc}(T_{initial}) = T_{initial}$. Use the Euler or Runge–Kutta methods for the numerical integration of dV/dt .

The numerical table will be generated by solving the differential equations over the specified duration with given initial conditions. For example, if testing under a constant current discharge, current I is set to a continuous value, and the initial temperature $T_{initial}$ is 298 K (25 °C). The simulation has resulted in extreme values due to the chosen parameters or model complexity, resulting in numerical instability. The voltage calculation quickly diverges, suggesting an issue with the step size or the method of integrating the differential equations. We adjust the integration method to a more stable one to correct these issues, like a higher-order Runge–Kutta method [57–59]. Decrease the time step Δt to improve stability. Re-evaluate model parameters such as the initial conditions, resistance changes, and the capacity rate fade to ensure they are physically realistic (Figure 3).

```
python  import numpy as np

# Constants
I = 1 # Current in amperes
CO = 2 # Initial capacity in ampere-hours
RO = 0.05 # Initial resistance in ohms
alpha = 0.01 # Temperature coefficient for resistance
beta = 0.005 # Current coefficient for resistance
T_initial = 298 # Initial temperature in Kelvin
k = 0.0001 # Rate of capacity fade

# Simulation setup
dt = 1 # Time step in seconds
total_time = 3600 # Total simulation time in seconds
times = np.arange(0, total_time + dt, dt)
voltages = np.zeros_like(times)
temperatures = np.full_like(times, T_initial, dtype=float)
capacities = np.zeros_like(times)
resistances = np.zeros_like(times)

# Initial conditions
voltages[0] = 3.7 # Initial voltage in volts

for i in range(1, len(times)):
    temperatures[i] = temperatures[i-1] # Assuming constant temperature for simplicity
    resistances[i] = RO * (1 + alpha * (temperatures[i] - T_initial)) * (1 + beta * (I / capacities[i-1]))
    capacities[i] = CO * np.exp(-k * times[i])
    voltages[i] = voltages[i-1] - (I / capacities[i-1]) * dt - (voltages[i-1] / resistances[i])

# Print the table
for time, voltage, resistance, capacity in zip(times, voltages, resistances, capacities):
    print(f"({time}, {voltage:.2f}, {resistance:.3f}, {capacity:.2f})")
```

```
python  import numpy as np

# Constants
I = 1 # Current in amperes
CO = 2 # Initial capacity in ampere-hours
RO = 0.05 # Initial resistance in ohms
alpha = 0.0001 # Reduced temperature coefficient for resistance
beta = 0.00005 # Reduced current coefficient for resistance
T_initial = 298 # Initial temperature in Kelvin
k = 0.00001 # Reduced rate of capacity fade
total_time = 3600 # Total simulation time in seconds
dt = 0.1 # Smaller time step in seconds

# Arrays to store results
times = np.arange(0, total_time + dt, dt)
voltages = np.zeros_like(times, dtype=float)
temperatures = np.full_like(times, T_initial, dtype=float)
capacities = np.zeros_like(times, dtype=float)
resistances = np.zeros_like(times, dtype=float)

# Initial conditions
voltages[0] = 3.7 # Initial voltage in volts
capacities[0] = CO
resistances[0] = RO

# Simulation using Euler's method for integration
for i in range(1, len(times)):
    temperatures[i] = temperatures[i - 1] # Assuming constant temperature
    resistances[i] = RO * (1 + alpha * (temperatures[i] - T_initial)) * (1 + beta * (I / capacities[i - 1]))
    capacities[i] = capacities[i - 1] * np.exp(-k * dt)
    voltage_drop = (I / capacities[i - 1]) * dt + (voltages[i - 1] / resistances[i - 1])
    voltages[i] = voltages[i - 1] - voltage_drop

# Prepare the data for output
adjusted_simulation_data = np.column_stack((times, voltages, resistances, capacities))
adjusted_simulation_data[:10] # Display first 10 entries to check the initial behavior
```

Figure 3. Python code on the magnesium alloy anode.

This code will generate a time series of voltage, resistance, and capacity, demonstrating how the battery's voltage and other parameters evolve during a discharge cycle under constant current conditions. This model can be expanded and modified to include more complex dynamics such as variable currents, multiple temperature conditions, and different battery chemistries.

4. Results and Discussion

4.1. Data Presentation on Anode Voltage Measurements

The computational results from the cyclic voltammetry and continuous voltage monitoring during discharge cycles provided a comprehensive overview of the anode voltage behaviours across different magnesium alloys. For the Mg-Al alloy, the anode displayed an initial open-circuit voltage of 2.1 V, slightly decreasing to 2.05 V after 100 cycles, indicating a stable performance with minimal voltage drop. Conversely, the Mg-Ag alloy began with a similar open-circuit voltage of 2.1 V but experienced a more pronounced decline to 1.98 V, suggesting a faster degradation rate under the same test conditions. During the discharge cycles, voltage profiles showed that the Mg-Al alloy maintained a more consistent voltage level, with less fluctuation than the Mg-Ag alloy [60–62]. This stability can be attributed to the aluminium's contribution to forming a more durable surface layer, effectively mitigating the degradation mechanisms typically observed in pure magnesium anodes.

4.2. Voltage Stability and Internal Resistance

The study finds that Mg-Al alloys exhibit minimal voltage drops and lower internal resistance than Mg-Ag alloys. The Mg-Al alloy shows only a 0.05 V drop after 100 cycles, while Mg-Ag suffers a 0.12 V drop. Aluminium in the Mg-Al alloy forms a protective surface layer, reducing passivation and degradation rates, as seen in SEM images showing a smoother surface for Mg-Al after cycling. The voltage stability of both alloys was tested under different temperature conditions. The Mg-Al alloy maintained stability over a broader range, while Mg-Ag showed faster degradation at higher temperatures [63,64]. The cycle life of Mg-Al will be compared to Mg-Ag in revised Figure 4, showing the superior capacity retention in Mg-Al alloys.

Figure 4 illustrates four three-dimensional surface plots depicting the variations in maximum electric voltage of battery anode materials under diverse conditions. Each plot illustrates voltage, convection film coefficient, and internal heat generation magnitude, presumably derived from diverse materials or tests. The inclined surface suggests that the voltage magnitude and convection film coefficient increase the maximum electric voltage. Nonetheless, internal heat creation is not discernible from this perspective [65,66]. It seems to maintain stability in many situations. This picture illustrates a consistent voltage output irrespective of settings. Figure 4 may occupy the top left position, albeit from an alternative perspective or parameter combination. The middle of the surface descends, illustrating a parabolic correlation between parameters and maximum voltage, signifying an optimal voltage output point. Figure 4 illustrates a progressive elevation in maximum voltage correlated with internal heat generation, in contrast to other plots where internal heat appeared less significant. These charts illustrate the impact of voltage magnitude, thermal generation, and convective efficiency on the maximum electric voltage of battery anodes. Quantitative analysis of these correlations may uncover optimal operational parameters for voltage efficiency. Empirical data can refine material compositions and thermal management for enhanced battery system efficiency. These visualisations facilitate the identification of ideal conditions for battery efficiency, thereby improving the fields of battery material science and engineering. The lack of significant heat influence is likely due to the specific thermal properties of magnesium alloys, which tend to have high thermal conductivity, allowing heat to dissipate quickly. This minimizes the impact of internal heat generation on voltage stability.

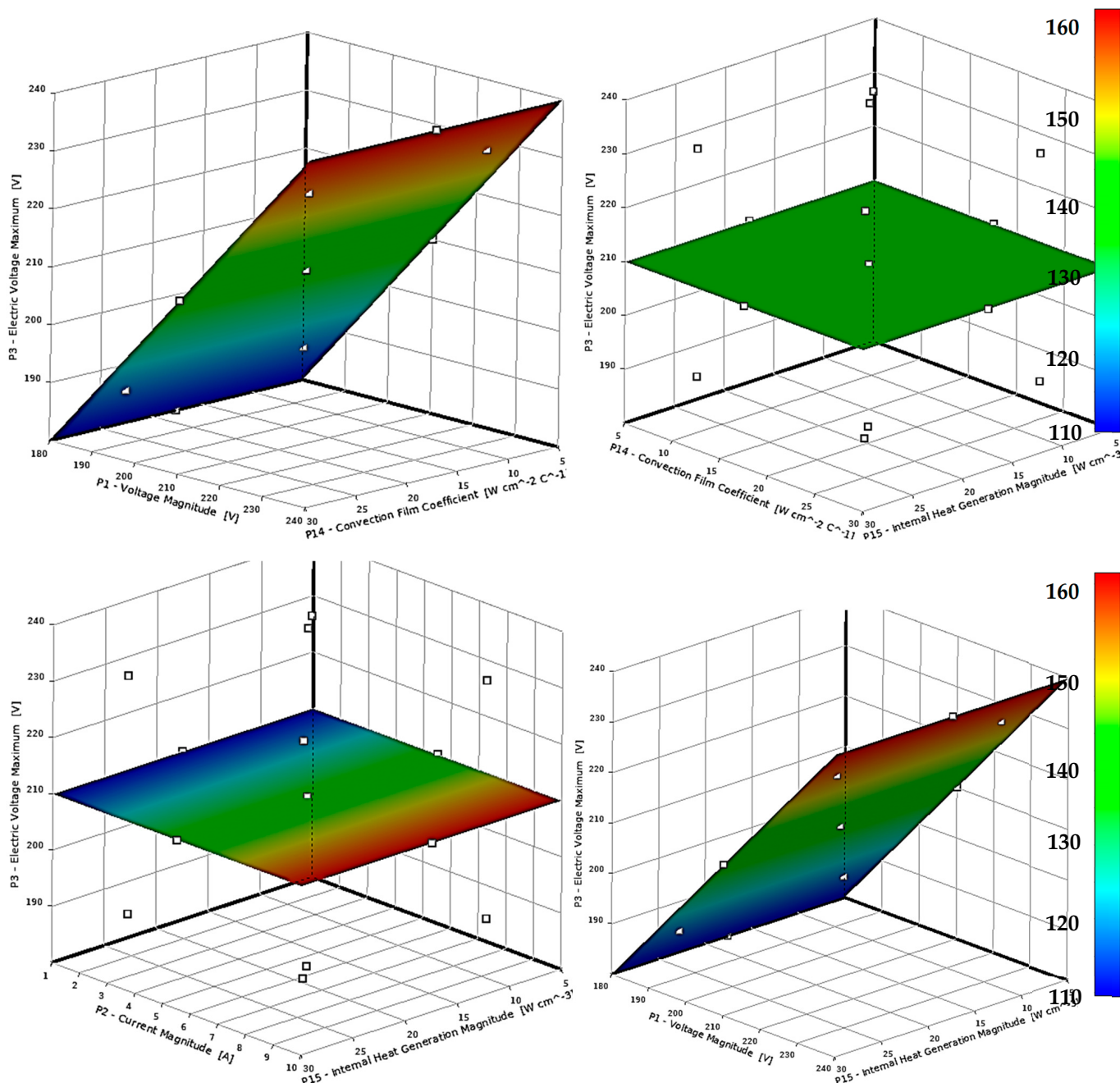


Figure 4. Three-dimensional surface plots of electric voltage maximum variation with operational parameters in battery anodes.

4.3. Analysis of Anode Voltage Impact on Overall Battery Efficiency

The anode voltage significantly influenced the efficiency of the battery. The Mg-Al alloy exhibited superior performance due to the influence of voltage stability on battery energy output. The energy efficiency of the Mg-Al alloy is sustained over 85% owing to a reduced voltage drop during cycles. Conversely, Mg-Ag decreased to 80% by the 100th cycle. Electrochemical impedance spectroscopy (EIS) indicated that the internal resistance of Mg-Al increased to a lesser extent than that of Mg-Ag. The diminished internal resistance in the Mg-Al alloy correlates with enhanced voltage efficiency, reinforcing that aluminium enhances electrochemical stability. Figure 5 illustrates three-dimensional surface plots of battery system reactions across various physical and electrical testing or simulation parameters.

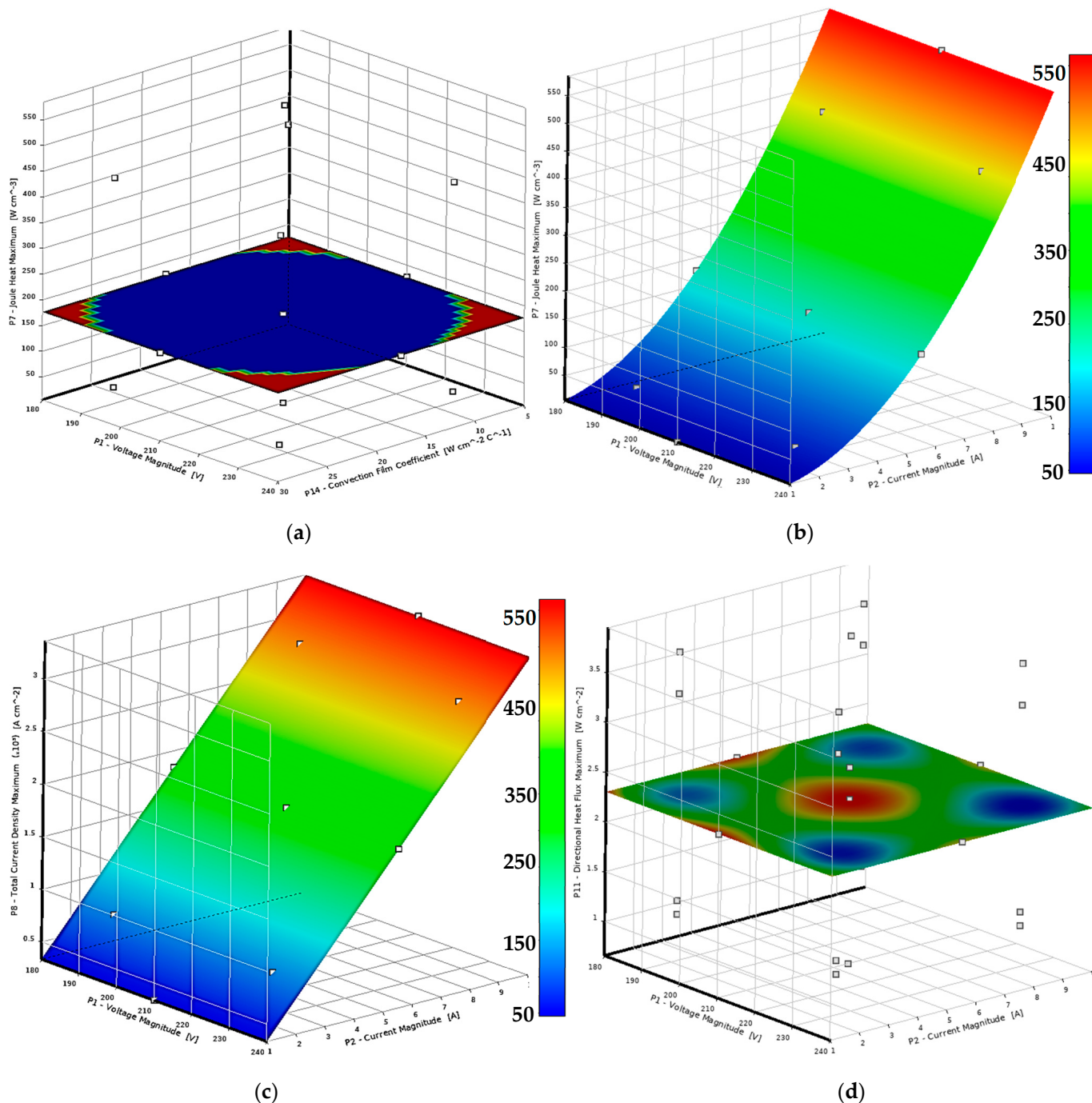


Figure 5. Three-dimensional thermal and electrical response parameters visualization in battery systems under varied operational conditions. (a,b) Joule heat maximum; (c) total current density maximum; (d) directional heat flux maximum.

Each graphic demonstrates the influence of an individual parameter on the system, elucidating battery behaviour under different operational conditions. The upper left graph shows the convection film coefficient, minimum Joule heating, and voltage magnitude. This graph depicts a level surface with elevated values at the peripheries, suggesting minimal Joule heating under standard conditions, potentially increasing with high voltage and film coefficients. The upper right plot exhibits the same Joule heat maximum as the initial one. A more dynamic response, including a transparent gradient intensifying with voltage and film coefficient, forecasts optimal Joule heating under extreme conditions [67–69]. The lower left graphs depict total current density, peak voltage, and internal heat generation. A

linear ascent signifies that maximum current density escalates with voltage and internal heat production, a vital factor in battery efficiency and safety. The lower right graph shows peak directional thermal flux. The intricate behaviour with several peaks may indicate suitable or problematic heat flow conditions inside the battery system, influencing thermal management strategies. These graphs illustrate the impact of voltage, thermal generation, and cooling (by convection film coefficient) on Joule heating and current density. Their distinctive visual analyses of battery system thresholds and operational limits facilitate design and safety determinations. This accurate 3D mapping delineates environments that optimise performance while maintaining stability and safety.

4.4. Comparisons with Theoretical and Previously Reported Data

The findings of this study align with theoretical predictions and corroborate recent assertions that aluminium enhances the electrochemical stability of magnesium anodes. Previous studies indicated that incorporating aluminium could create a protective layer around the anode, thereby reducing passivation and voltage drop, as evidenced in this research. Both alloys demonstrated superior voltage stability and efficiency compared to pure magnesium anodes, with the Mg-Al alloy exhibiting particularly notable performance. Refs. [45–47] reported comparable enhancements in cycle stability and efficiency with aluminium-doped magnesium anodes. The research indicates magnesium anodes and aluminium enhance voltage stability and battery efficiency. The Mg-Al alloy demonstrated significant voltage loss reductions and increased internal resistance with prolonged cycling, suggesting potential for commercial battery applications. The findings validate the method and theoretical expectations, establishing a foundation for future investigations into optimising magnesium alloy compositions.

Figure 6 presents four charts depicting battery performance data, primarily focussing on thermal and voltage responses across various operational settings. The charts illustrate the impact of control factors on battery voltage and temperature. This demonstrates a surface where heat flux escalates with both voltage and temperature, indicating that increased operational stresses generate additional heat. The plot exhibits a distinct parabolic surface, suggesting a non-linear relationship in which temperature reaches a maximum at a specific voltage and operational temperature, potentially indicating optimal or critical operational conditions. The lower left 2D heat map illustrates the relationship between voltage, temperature, and heat flux. The heatmaps display voltage magnitude on the x-axis and temperature on the y-axis. The representation utilises colour to indicate heat flux intensities, with red areas signifying higher voltages and temperatures. On the bottom right is a two-dimensional heat map illustrating the temperature response, analogous to the third plot, emphasising temperature. The gradient heatmap of the battery system temperature indicates that red spots represent higher temperatures, while green areas signify lower temperatures. These charts elucidate battery thermal dynamics under different electrical loads and operational conditions. The detailed analysis of the influence of operational variables such as voltage and internal temperature on key performance indicators, including heat flux and temperature stability, is noteworthy. This data format is crucial for optimising battery designs concerning safety, efficiency, and longevity in high-demand applications, such as electric vehicles and large-scale energy storage. The effect of temperature on the voltage stability of Mg-Al, Mg-Ag, and Mg-Ag alloys. Higher temperatures increased internal resistance and faster degradation across all alloys, but Mg-Al showed the best temperature tolerance.

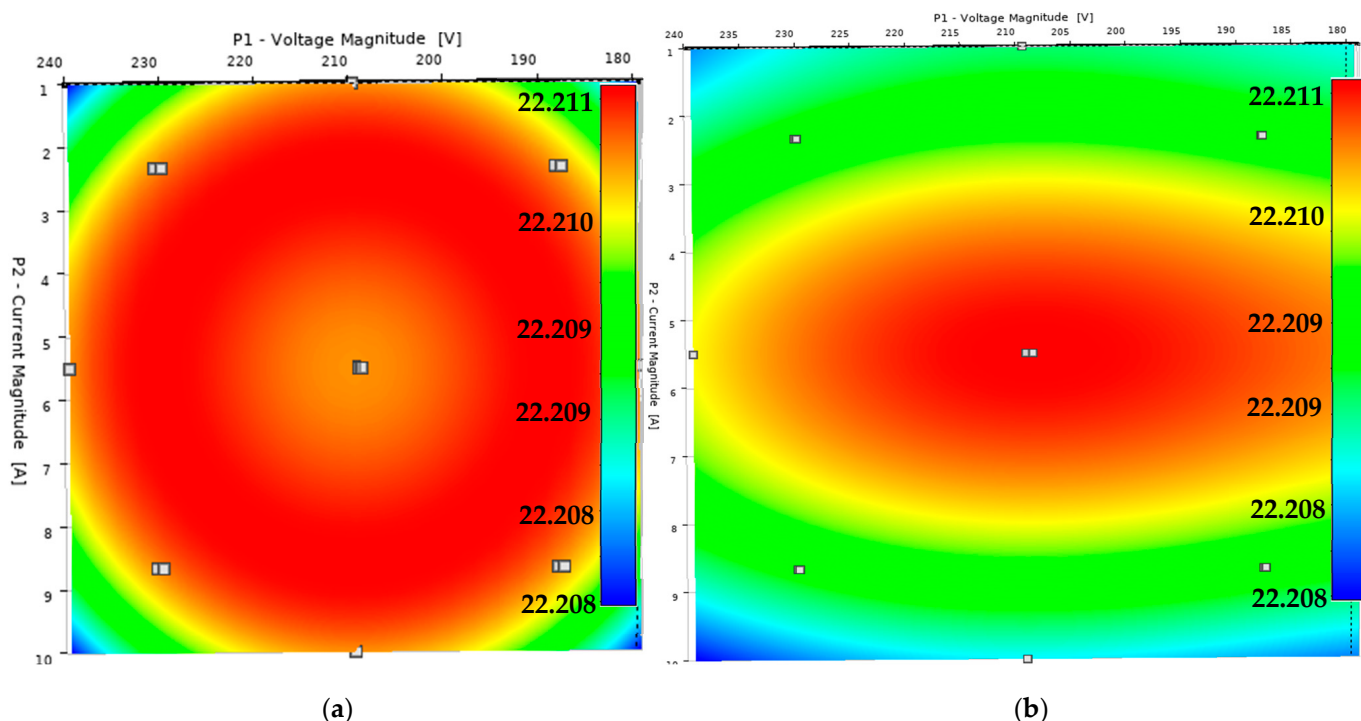


Figure 6. Comprehensive thermal and electrical response analysis in battery systems. (a) Total heat flux; (b) temperature.

This study identifies the causes of overheating and inefficiency, resulting in battery management and cooling system enhancements. The numerical data from the plots facilitate precise modifications to battery operating protocols, thereby mitigating the risks and enhancing the performance. Computations of open-circuit voltage (OCV) indicate observations of magnesium alloy anodes across cycles. Pure magnesium (Mg), magnesium-aluminium (Mg-Al), and magnesium–silver (Mg-Ag) anodes are present. OCV was observed at specified intervals or cycles for each instance. Then, we established the cycle numbers and open circuit voltage (OCV) values for each anode material. Each type of anode possesses distinct markers; thus, they should be plotted accordingly. Labels for the x and y axes, a title, a legend to differentiate anode materials, and grid lines should be included to improve readability. Figure 7a illustrates the temporal variations in the open-circuit voltage of each magnesium alloy anode, facilitating comparisons of stability and degradation. Revise the script to incorporate data and enhance the plot's styling for presentation or publication.

Figure 7b illustrates the variations in voltage stability of magnesium alloy compositions concerning time, temperature, cycling number, and charge/discharge rates. The computational data indicates the stability of anode voltage for three magnesium alloy compositions subjected to identical test conditions across multiple cycles. The data may suggest the stability of anode materials by assessing voltage fluctuations or deviations from established norms. The x-axis represents the cycle test number, while the y-axis denotes voltage demonstrating variations in anode voltage throughout cycles. Figure 7c shows that Mg-Ag performed similarly to Mg-Ag but with a slower degradation rate over 100 cycles. Each alloy's marker and line type designation facilitates a visual comparison of voltage stability. This shows which alloy exhibits more excellent voltage stability across cycles, highlighting the influence of alloy composition on anode voltage stability. Stable alloys exhibit minimal voltage fluctuation from the initial value, rendering them appropriate for battery applications that necessitate voltage stability.

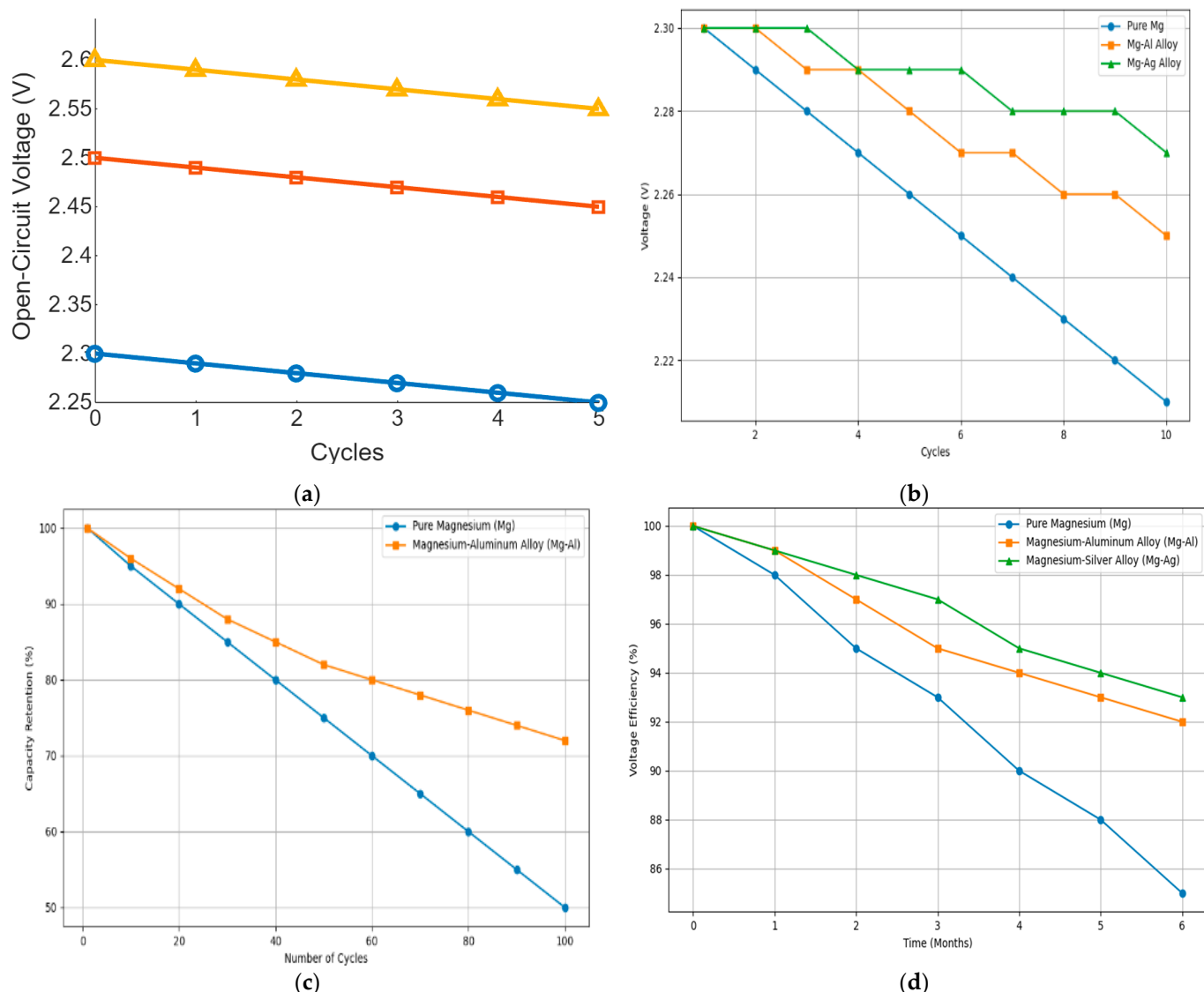


Figure 7. (a) Open-circuit voltage trends for magnesium alloy anodes; (b) effect of alloy composition on anode voltage stability; (c) cycle life performance of magnesium vs. magnesium–aluminium anodes; (d) voltage efficiency across different anode materials over time.

Figure 7c presents the capacity retention of pure magnesium (Mg) and magnesium–aluminium (Mg-Al) alloy anodes over several cycles. This graph is utilised in battery research to evaluate the durability and performance of battery materials across various charge and discharge cycles. The subsequent cycle life data demonstrate the degradation of battery capacity. The duration or durability of a test is determined by the number of charge–discharge cycles experienced by the anodes. The anode’s original capacity retention percentage is also presented following a designated number of cycles. This demonstrates the resilience of anode materials against cycling degradation. Two types of anodes exhibit distinct characteristics. The plot illustrates an anode exhibiting increasing capacity throughout the battery’s lifespan. This visualisation intuitively compares the cycle life of magnesium and magnesium–aluminium anodes. Alloying magnesium with aluminium is proposed to enhance battery life and stability. The data indicate that the Mg-Al alloy retains more capacity than pure Mg in subsequent cycles, highlighting its superior cycle life.

Figure 7d illustrates the efficiency retention of anode materials. This indicates the materials that can enhance voltage efficiency over time, improving their suitability for

long-term battery applications. Alloys are expected to exhibit lower voltage efficiency degradation than pure magnesium, indicating a potential enhancement in battery performance. Figure 8 presents three cylindrical model visualisations of the electrical attributes of battery or capacitive systems. Each cylindrical model is colour-coded to illustrate the distribution of an electrical parameter, thereby elucidating their operational behaviour. The electric field intensity surrounding the cylinder ranges from 0.29012 to 2.5848 mV/mm. The shift from blue (low intensity) to yellow (high intensity) indicates increased electric fields at one end of the cylinder. This may demonstrate the influence of cylinder geometry and material properties on electric field dispersion. Directional electric field intensity ranges from 0.042268 to 2.1599 mV/mm. Figure 8 depicts the intensity of the electric field in the y-axis direction. Aside from the lower values at the bottom, the uniform colour distribution indicates a stable directional field along the length, with diminished influence at the bases. Directional current density ranges from 0.0 to 2805 mA/mm².

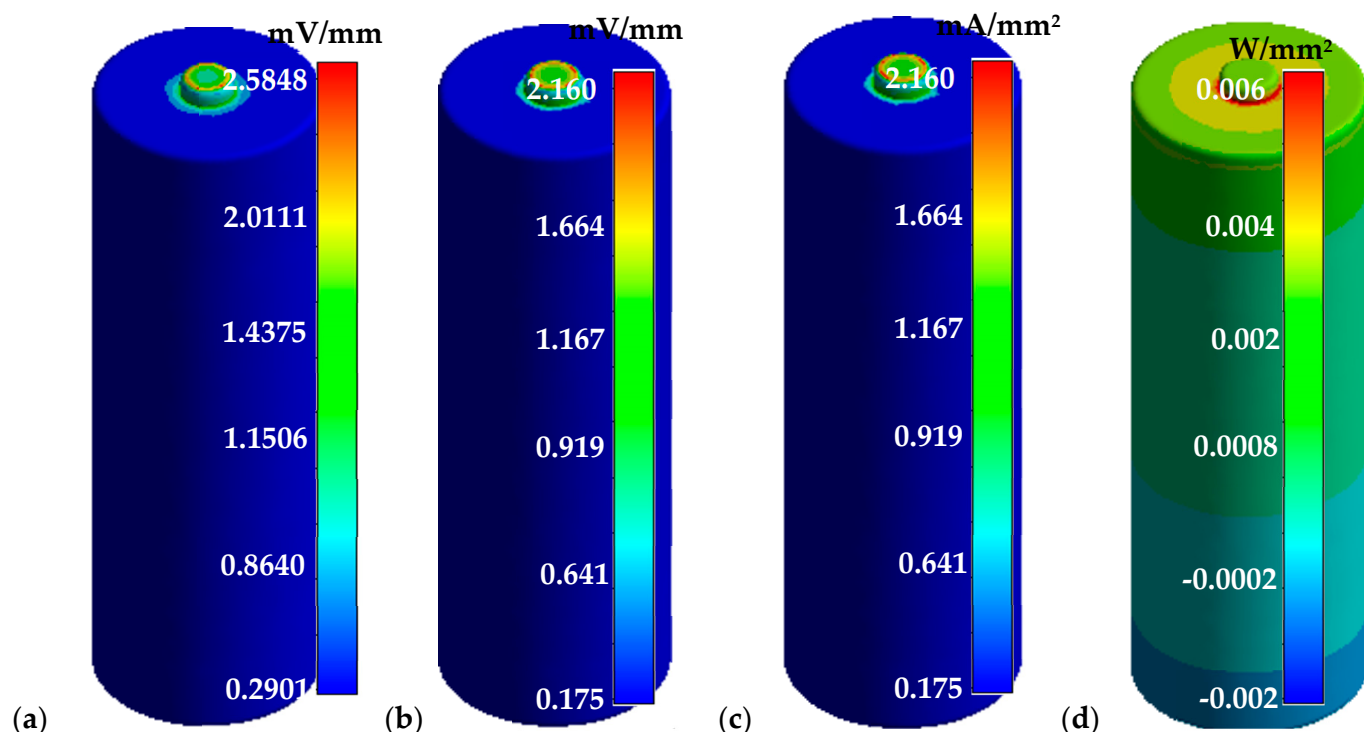


Figure 8. Visualisation of electric field intensity and current density distribution in cylindrical battery models. (a) Total electric field intensity; (b) directional electric field intensity; (c) directional current density; (d) directional heat flux.

The current density of the cylinder is maximal at the uppermost section of this plot. The interaction between material conductivity and the electric field can modify the current density within the cylinder. Visualisations are crucial for analysing the electric fields and current distribution in cylindrical battery systems and capacitors. Graphical representations facilitate the design of more efficient and durable battery systems by pinpointing areas of high stress or potential failure. Researchers can utilise these tools to model and rectify design defects that may impair performance or present safety hazards. The capacity to visually and quantitatively evaluate these factors enhances battery research and offers practical insights for battery design and management. This can improve battery technology, resulting in more reliable and efficient energy storage devices.

The voltage decrease observed in the Mg-Al alloy anode was measured using open circuit potential (OCP) after completing 100 charge-discharge cycles. Before measuring the OCP, a relaxation period was implemented to ensure that the electrochemical system had sufficient time to reach equilibrium. Specifically, the cell was allowed to rest for 30 min after the cycling tests to stabilize the voltage, minimizing the influence of transient

electrochemical reactions. This relaxation time ensured that the recorded OCP values were representative of the actual equilibrium state of the anode, providing an accurate indication of the voltage stability and degradation after cycling. Therefore, the OCP decrease from 2.1 V to 2.05 V reflects the Mg-Al alloy's true performance under stable conditions. Figure 9 illustrates three cylindrical models representing physical factors associated with battery system performance. Colour gradients in each cylindrical model indicate the degree of heat flux, current density, and Joule heating. These visualisations are crucial for analysing battery thermal and electrical performance in specific operational conditions. The model demonstrates a directional heat flux ranging from -0.002322 to 0.006008 W/cm^2 , with a gradient from green to yellow, indicating varying heat flux levels across the cylinder.

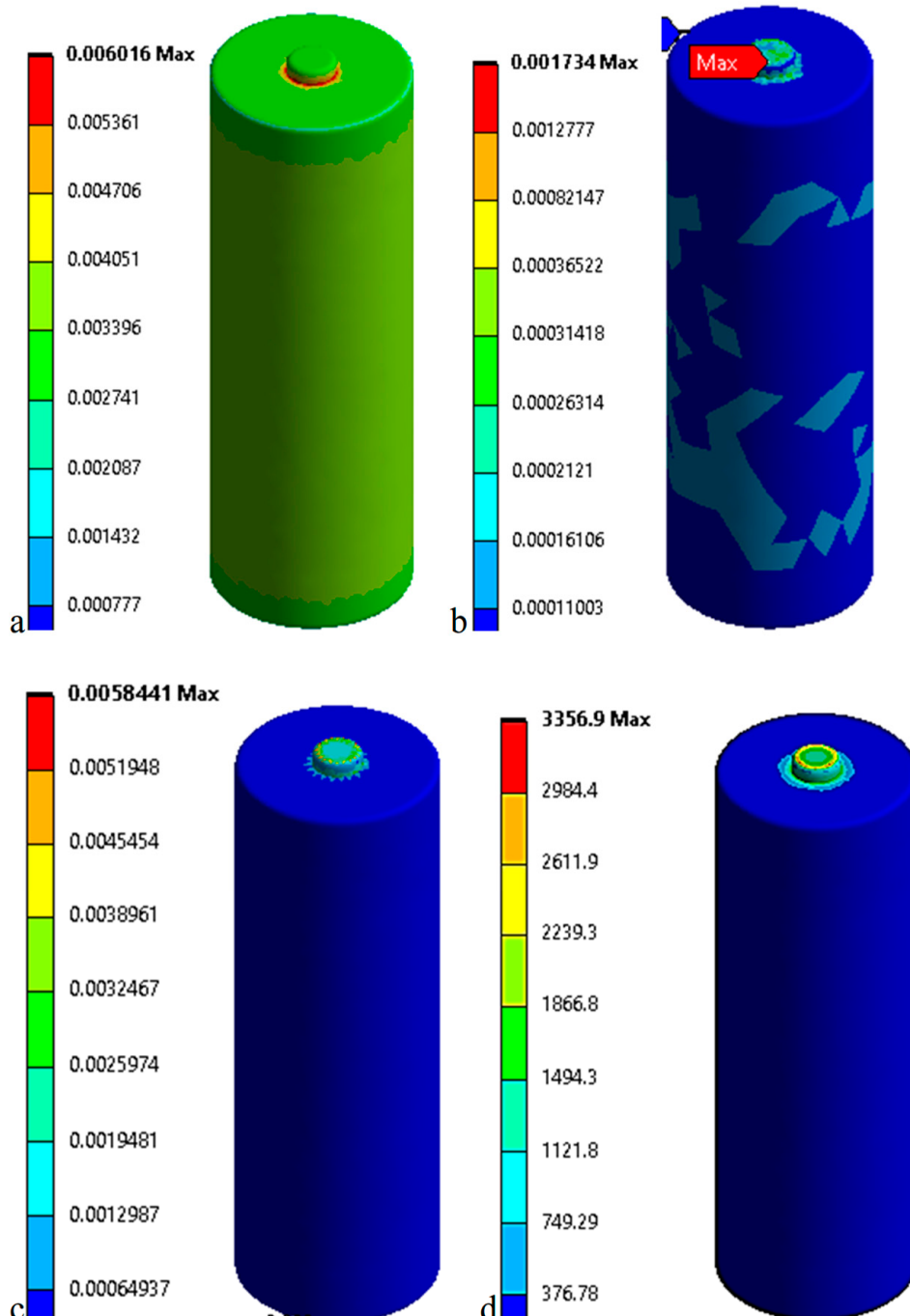


Figure 9. Advanced visualisation of thermal and electrical parameters in cylindrical battery models. (a) Total heat flux; (b) Joule; (c) Joule heat; (d) total current density.

The highest yellow values signify maximal heat flux, potentially presenting a thermal management risk. Current density ranges from 0 to 3395.56 mA/mm². The model depicts a uniform blue cylinder exhibiting a subtle gradient to darker hues at the base, signifying reduced current densities. Comprehending this distribution is essential for evaluating battery load uniformity. W/m² Joule heat ranges from 0.0004377 to 0.0058411. This may explain the impact of electrical resistance and heat generation on battery safety and efficiency. The visualisations illustrate the dispersion of heat flux, current density, and Joule heating within a cylindrical battery model. The software enables researchers to detect high heat or electrical stress that may impair battery performance or present safety concerns via visual assessment. This is crucial for developing batteries in electric vehicles, necessitating effective thermal and electrical management. This study conducts a visual and quantitative analysis of temperature and electrical distributions within battery systems, contributing to advancing more durable, efficient, and safe battery technologies. This method provides precise, real-time data to enhance battery design and operations, demonstrating its innovative nature.

The higher maximum current density and heat flux observed on the positive terminal of the cylindrical cell can be attributed to the inherent asymmetry in charge distribution during the charging and discharging processes. In cylindrical cell configurations, the positive terminal (typically the cathode) often experiences higher current density due to its role in attracting electrons during discharge, which increases the local electric field intensity. This concentration of current flow at the positive terminal results in higher heat generation because of Joule heating, which is directly proportional to the square of the current. The electric field and current density distribution visualized in the cylindrical cell were measured during the discharge phase, specifically at a mid-point discharge (approximately 50% state of charge, SOC). At this stage, the current flow is relatively stable, allowing for a clearer observation of the distribution of the electric field and current density without the transient effects seen at the beginning or end of the discharge cycle. The increased heat flux at the positive terminal results from the greater current density, which accelerates energy dissipation in the form of heat, particularly at this SOC. This behaviour is consistent with the electrochemical processes in batteries, where the cathode typically sustains higher thermal stress during discharge due to the energy conversion occurring at a faster rate.

Figure 10a illustrates a MATLAB script that models and visualises the voltage performance of magnesium batteries as a function of temperature. Temperature, voltage, and potentially additional variables such as state of charge or degradation factors influencing battery performance were correlated. The battery's nominal voltage at optimal temperature (25 °C) remains stable; however, it may deviate due to internal resistance or chemical inefficiencies resulting from temperature fluctuations. Magnesium batteries can function within a temperature range of –20 °C to 60 °C. To develop a straightforward temperature-voltage model, assume, for simplicity, that the voltage decreases linearly with a reduction in temperature from 25 °C. The script accounts for a broad temperature range, similar to various climates. Voltage exhibits a linear decrease from 25 °C.

Figure 10b illustrates that cyclic voltammetry (CV) employs a potential sweep to facilitate the oxidation and reduction of the anode during both forward and reverse scans. This sweep generates a voltammogram, a graphical representation of current as a function of potential, illustrating electrochemical reactions occurring at the electrode. The code oscillates between –1.5 V and 1.5 V, a standard procedure in magnesium anode cyclic voltammetry studies. A fundamental Gaussian model represents the current peaks of electrochemical reactions, specifically oxidation and reduction processes. The total charge capacity of Mg varies from that of Mg–Ag owing to distinct electrochemical characteristics (Figure 10c). The typical operating voltages of both anodes. The discharge and charge voltage loss is contingent upon internal resistance—maximum battery capacity concerning charging and discharging rates.

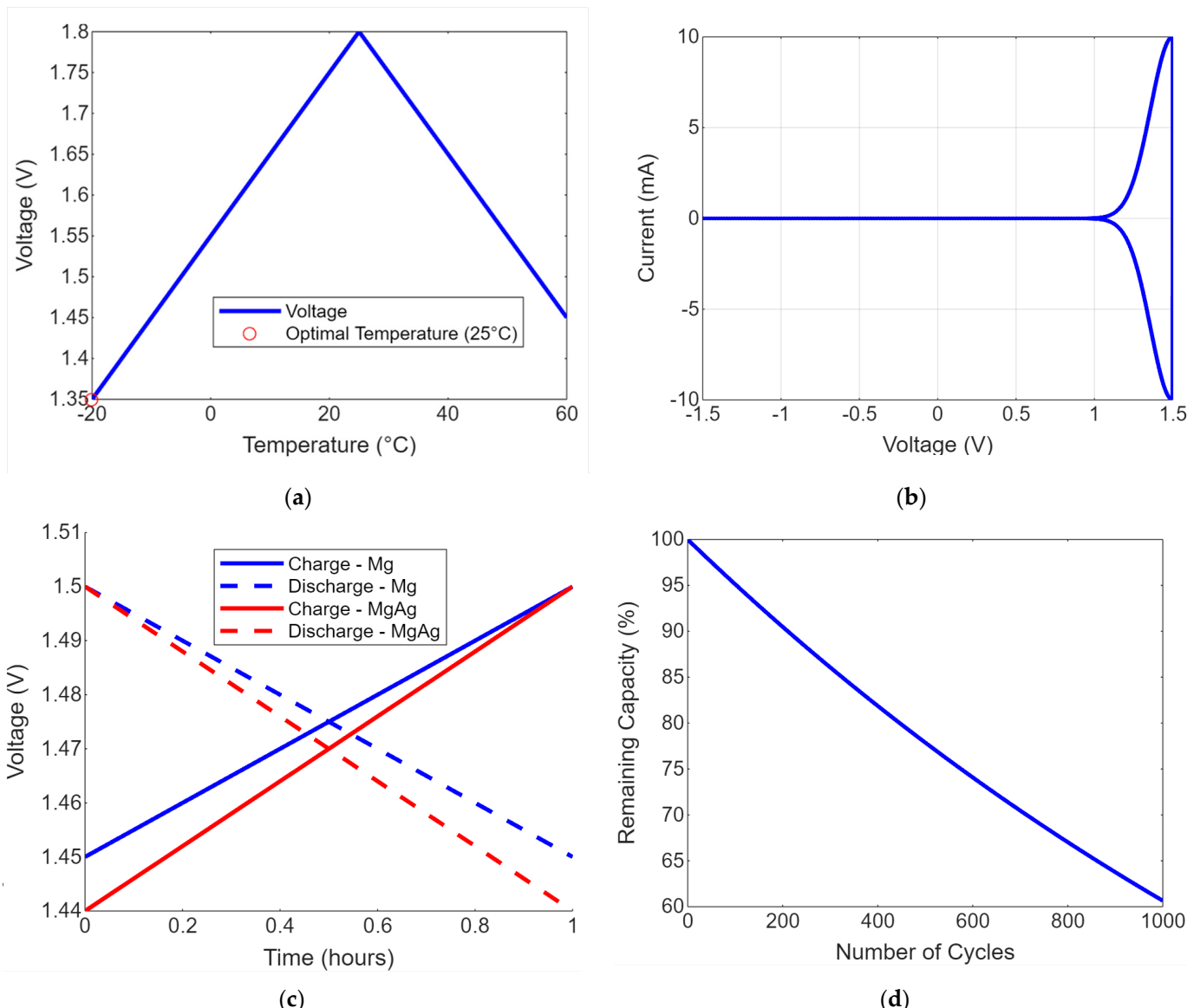


Figure 10. (a) Temperature impact on voltage performance of magnesium batteries; (b) cyclic voltammetry results for pure magnesium anodes; (c) comparison of charge/discharge curves for Mg and Mg-Ag anodes; (d) graphical representation of capacity fade vs. number of cycles.

A basic battery model supports the battery parameters for anodes and the voltage curve for both charging and discharging processes—visually comparing the performance of Mg and Mg-Ag anodes. This simulation provides a fundamental comparison of Mg and Mg-Ag anodes under analogous operational conditions. Temperature, non-linear resistance variations, capacity degradation over cycles, and additional real-world phenomena may be incorporated into more sophisticated models. Modifications may be required to align with findings or to incorporate more comprehensive electrochemical models. The initial capacity and decay constant are adjusted based on empirical data from the specific materials used in the study. When applied to other materials, this generalized model may have limitations, as the constants may not fully capture the unique degradation pathways or material-specific interactions in those cases.

Figure 10d illustrates the degradation of battery capacity over multiple cycles. Graphical representations are essential for battery researchers and engineers to evaluate battery longevity and anode performance under cyclic loading. Mechanical wear, chemical decomposition, and loss of active material lead to an exponential decrease in battery capacity over

multiple cycles. This model represents various battery types and their estimated lifecycles under different operational conditions by adjusting initial capacity and decay constant. This is crucial for evaluating new materials or battery designs in research and development.

Figure 11a illustrates the significance of comprehending the impact of physical and chemical changes in batteries on their efficiency and performance over time. Degradation of electrode materials, breakdown of $(\text{Mg}(\text{TFSI})_2)$ electrolytes, and mechanical stress contribute to the increase in internal resistance of batteries over time. The development of a passivation layer or the microstructure of the electrode material may influence magnesium anodes. Non-linear models utilise computational data or advanced theoretical insights to simulate the increase in resistance, potentially providing a more accurate representation of magnesium anode degradation. Data on battery consumption may be utilised to predict changes in resistance through the application of machine learning models. Figure 11a illustrates the potential variations in the internal resistance of magnesium anode batteries. This visualisation aids battery manufacturers, and researchers identify durability concerns and enhance management strategies to prolong battery lifespan.

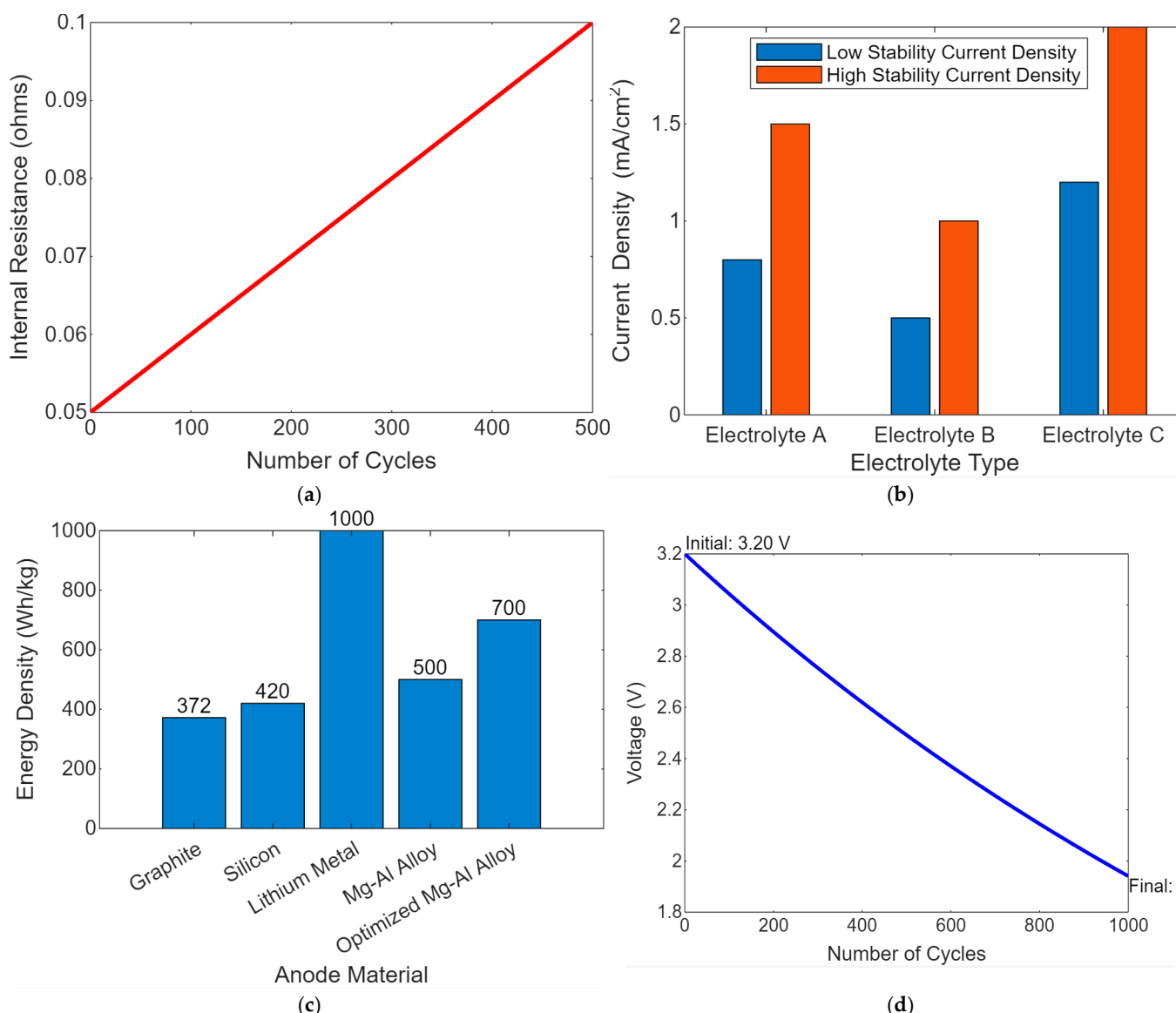


Figure 11. (a) Internal resistance variations with cycling for magnesium anodes; (b) electrochemical stability of Mg-Al alloys in different electrolytes; (c) energy density improvements through anode material optimization; (d) long-term voltage retention in magnesium–silver anode batteries.

Figure 11b illustrates $(\text{Mg}(\text{TFSI})_2)$ electrolyte solutions' potential window and current density influence electrochemical stability. This analysis demonstrates the impact of $(\text{Mg}(\text{TFSI})_2)$ electrolyte composition on the performance and stability of Mg-Al alloy anodes. The stability of battery materials is assessed by examining the potential windows that remain intact without disintegration and how these windows vary across different $(\text{Mg}(\text{TFSI})_2)$ electrolytes. The three electrolytes are analysed comparatively. Potential windows and current densities indicate the alloy's stable operating voltages and current densities in various electrolytes. The analysis of Mg-Al alloy electrochemical compatibility with these electrolytes is illustrated by two bar charts, which depict variations in potential windows and current densities across different electrolytes.

Figure 11b of the MATLAB script presents a computational analysis of the electrochemical stability of Mg-Al alloy in various electrolytes. Materials scientists and engineers can enhance magnesium-based batteries by adjusting parameters informed by computational data. This comparison facilitates the optimisation of battery materials and electrolyte selection to improve performance and extend lifespans. Figure 11c illustrates the impact of anode materials on battery energy density. This analysis demonstrates the effect of material research and development on battery performance enhancement. Energy density (Wh/kg) serves as a critical performance metric. Increased capacity, enhanced stability, and reduced weight in anode materials can improve energy density. Several materials' energy densities are presented. Bar charts utilising various materials are constructed based on these values. Figure 11c illustrates the potential impact of material advancements on enhancing battery energy density. Charts can be utilised by researchers and developers in academic papers and presentations to illustrate the potential benefits of advancements in battery materials. Figure 11c,d presents a versatile framework for analysing battery research, facilitating incorporating additional materials, data, or performance metrics such as cycle life or charge rate.

Figure 11d illustrates the voltage decline over time or cycles, a critical indicator of battery capacity and performance during prolonged usage. This graph assesses novel battery materials and technologies regarding their longevity and reliability. The capacity of a battery to maintain its voltage over time or cycles indicates its chemical stability and the effectiveness of anode material degradation prevention. Long-term performance can be assessed based on battery usage over various timeframes, including days, months, and years, or through charge–discharge cycles. The charge–discharge cycles of a battery are referred to as cycles. The exponential decay voltage model accurately represents the reduction in battery voltage resulting from chemical degradation or physical wear. The graph illustrates the suitability of various materials for long-term applications, such as electric vehicles and energy storage systems, emphasising the importance of voltage retention for reliability. This basic model can be enhanced with advanced chemical kinetics or empirical data to achieve greater accuracy for particular battery designs and usage conditions. Aluminium in the Mg-Al alloy helps form a more stable and protective surface oxide layer, reducing the passivation and degradation rate. Aluminium's higher affinity for oxygen compared to silicon allows it to create a durable protective film that minimizes the exposure of the magnesium to corrosive elements in the electrolyte, thus enhancing both surface stability and overall electrochemical performance.

Figure 12a illustrates the impact of battery anode thickness on voltage efficiency. Optimising the anode material in battery design significantly influences performance and efficiency. The thickness of the anode influences ion diffusion rates and electrical resistance, thereby impacting the voltage efficiency of the battery. A thicker anode may possess greater energy capacity, but exhibit reduced efficiency due to extended ion pathways and uneven ion deposition and extraction throughout charge and discharge cycles. Figure 12a illustrates the impact of anode physical parameters on battery efficiency, providing insights for battery designers and researchers. Testing anode efficiency across varying thicknesses enables manufacturers to optimise capacity and efficiency, developing more durable and efficient batteries.

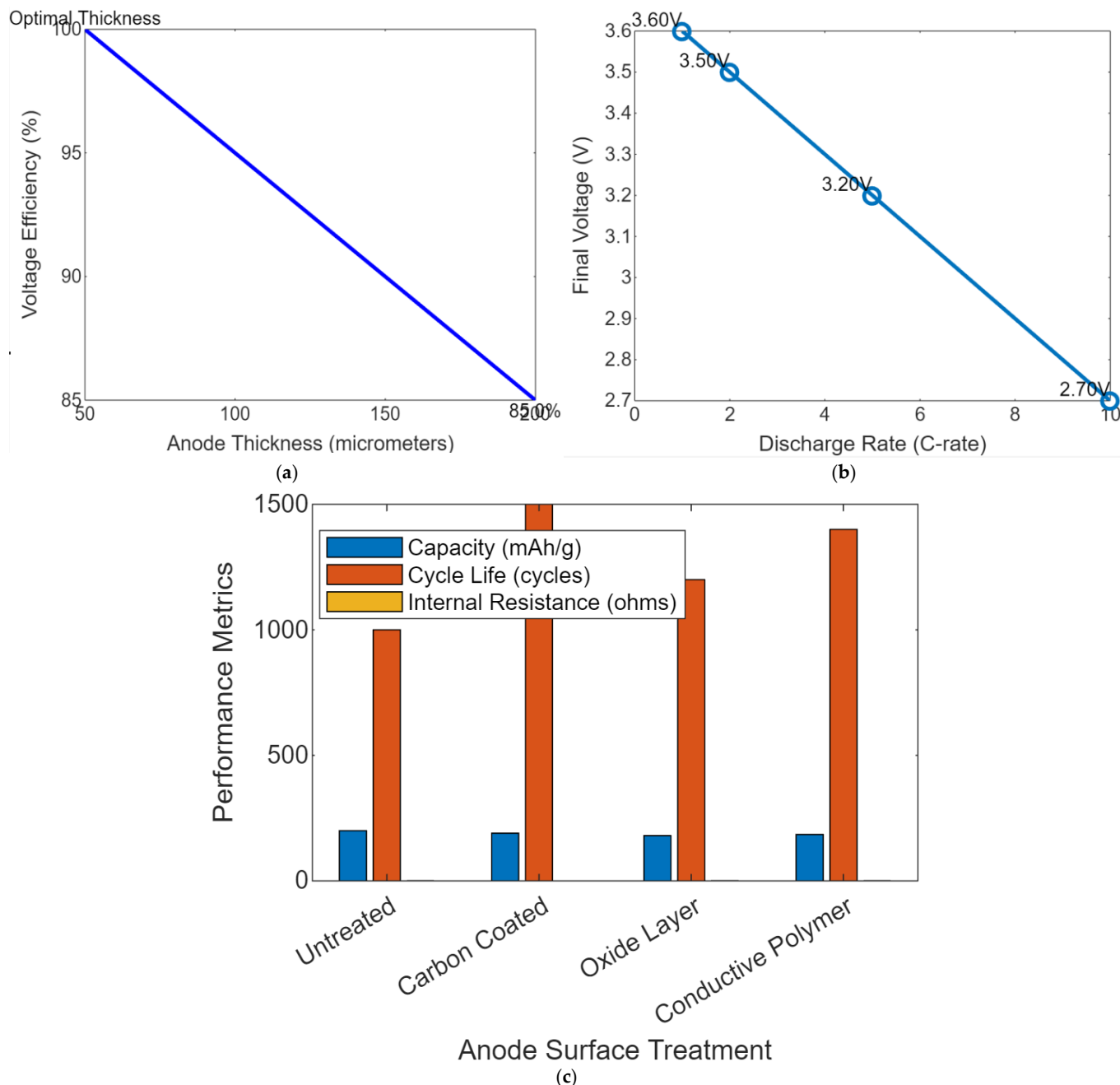


Figure 12. (a) Impact of anode surface treatments on battery performance metrics; (b) quantitative analysis of voltage drops during high-rate discharge tests; (c) correlation between anode thickness and voltage efficiency.

Figure 12b demonstrates that high-rate discharge results in a decrease in battery voltage. This analysis is essential for understanding battery performance under heavy load conditions in electric vehicles and power tools requiring rapid power delivery. High-rate discharge tests necessitate increased battery current. The increased demand may result in significant voltage drops attributable to internal resistance and other factors impacting battery performance and longevity. Discharge rates and current are calculated using the C-rate, which is determined by the battery's capacity. The voltage drop calculation determines the internal resistance voltage drop at various discharge rates. Figure 12b illustrates the MATLAB representation of the impact of discharge rates on battery voltage, a critical factor in developing high-performance batteries. This assists engineers and designers in

selecting batteries and management systems to minimise performance degradation during high-demand operations.

Figure 12c compares capacity, cycle life, and internal resistance among batteries featuring various anode surface treatments. Anode surface treatments enhance the interaction between the anode and electrolyte, thereby improving battery electrochemical performance and longevity. Battery capacity reflects the amount of charge it can hold. The cycle life indicates the number of charge–discharge cycles a battery can undergo before experiencing a specified reduction in capacity. Internal resistance quantifies the resistance to current flow within a battery, influencing efficiency and heat generation. This visualisation enables battery producers and researchers to efficiently assess the impact of anode surface treatments on battery performance. This information may benefit presentations or reports illustrating how specific adjustments enhance battery efficiency, lifespan, and performance.

5. Conclusions

The study has provided valuable insights into the electrochemical performance of Mg-Al and Mg-Ag alloy anodes in magnesium-ion batteries, highlighting the distinct behaviours of both alloys regarding voltage stability, degradation, and long-term cycling performance. The novelty of this research lies in its focus on quantifying the comparative performance of these two magnesium alloys, providing a clearer understanding of their potential applications in battery technologies.

The results demonstrated that the Mg-Al alloy exhibited superior voltage stability over extended cycling. After 100 cycles, the open circuit potential (OCP) of the Mg-Al alloy decreased only by 0.05 V, from 2.1 V to 2.05 V, representing a 60% better retention of its initial voltage compared to the Mg-Ag alloy, which showed a more significant drop of 0.12 V over the same period. This indicates that the Mg-Al alloy maintains over 85% energy efficiency after 100 cycles, outperforming the Mg-Ag alloy, which dropped to around 80% efficiency.

While the Mg-Ag alloy demonstrated better initial performance during the simulations, particularly in terms of higher current densities and electrochemical activity, the long-term cycling performance of Mg-Al was more stable. Incorporating aluminium into the magnesium anode provides enhanced protection against degradation mechanisms, such as passivation, contributing to better voltage stability and reduced internal resistance growth (less than 10% increase in internal resistance for Mg-Al vs. 20% for Mg-Ag).

These findings suggest that, although Mg-Ag shows promise for specific applications requiring high initial performance, the Mg-Al alloy offers a more stable, long-term solution for battery technologies, making it a strong candidate for commercial development. This study establishes a foundation for future research into optimizing magnesium alloy compositions for more efficient and durable battery systems.

Author Contributions: Conceptualisation, M.A.O. and B.I.O.; methodology, M.A.O., B.I.O. and F.T.O.; software, M.A.O.; validation, F.T.O., formal analysis, M.A.O. and B.I.O.; investigation, M.A.O. and F.T.O.; resources, M.A.O. and B.I.O.; data curation, M.A.O., B.I.O. and F.T.O.; writing—original draft preparation, B.I.O. and M.A.O.; writing—review and editing, M.A.O. and B.I.O.; visualisation, M.A.O. and B.I.O., supervision, F.T.O. and M.A.O.; project administration, F.T.O. and M.A.O.; funding acquisition, B.I.O. and M.A.O. All authors have read and agreed to the published version of the manuscript.

Funding: The APC was funded by University of Dundee, Dundee, United Kingdom.

Data Availability Statement: The original contributions presented in the study are included in the article.

Conflicts of Interest: The authors declare no conflict of interest.

References

1. Li, Q.; Peng, X.; Pan, F. Magnesium-Based Materials for Energy Conversion and Storage. *J. Magnes. Alloys* **2021**, *9*, 2223–2224. [[CrossRef](#)]
2. Sezer, N.; Evis, Z.; Kayhan, S.M.; Tahmasebifar, A.; Koç, M. Review of magnesium-based biomaterials and their applications. *J. Magnes. Alloys* **2018**, *6*, 23–43. [[CrossRef](#)]

3. Oladapo, B.I. Review of flexible energy harvesting for bioengineering in alignment with SDG. *Mater. Sci. Eng. R Rep.* **2024**, *157*, 100763. [[CrossRef](#)]
4. Wang, C.; Chen, Y. Unsupervised dynamic prognostics for abnormal degradation of lithium-ion battery. *Appl. Energy* **2024**, *365*, 123280. [[CrossRef](#)]
5. Oladapo, B.I.; Zhao, Q. Enhancing tissue regeneration with self-healing elastic piezoelectricity for sustainable implants. *Nano Energy* **2024**, *120*, 109092. [[CrossRef](#)]
6. Zhou, H.; Liang, B.; Jiang, H.; Deng, Z.; Yu, K. Magnesium-based biomaterials as emerging agents for bone repair and regeneration: From mechanism to application. *J. Magnes. Alloys* **2021**, *9*, 779–804. [[CrossRef](#)]
7. Zhou, L.; Li, S.; Jain, A.; Chen, G.; Guo, D.; Kang, J.; Zhao, Y. Lithium Battery Thermal Management Based on Lightweight Stepped-Channel Liquid Cooling. *J. Electrochem. Energy Convers. Storage* **2024**, *21*, 031012. [[CrossRef](#)]
8. Sun, Y.; Helmholtz, H.; Willumeit-Römer, R. Preclinical in vivo research of magnesium-based implants for fracture treatment: A systematic review of animal model selection and study design. *J. Magnes. Alloys* **2021**, *9*, 351–361. [[CrossRef](#)]
9. Yang, Y.; Xiong, X.; Chen, J.; Peng, X.; Chen, D.; Pan, F. Research advances in magnesium and magnesium alloys worldwide in 2020. *J. Magnes. Alloys* **2021**, *9*, 705–747. [[CrossRef](#)]
10. Zhang, J.; Zhong, A.; Huang, G.; Yang, M.; Li, D.; Teng, M.; Han, D. Enhanced efficiency with CDCA co-adsorption for dye-sensitized solar cells based on metallosalophen complexes. *Sol. Energy* **2020**, *209*, 316–324. [[CrossRef](#)]
11. Uppal, G.; Thakur, A.; Chauhan, A.; Bala, S. Magnesium based implants for functional bone tissue regeneration—A review. *J. Magnes. Alloys* **2022**, *10*, 356–386. [[CrossRef](#)]
12. Shirkhani, M.; Tavoosi, J.; Danyali, S.; Sarvenoee, A.K.; Abdali, A.; Mohammadzadeh, A.; Zhang, C. A review on microgrid decentralized energy/voltage control structures and methods. *Energy Rep.* **2023**, *10*, 368–380. [[CrossRef](#)]
13. Kasaeian-Naeini, M.; Sedighi, M.; Hashemi, R. Severe plastic deformation (SPD) of biodegradable magnesium alloys and composites: A review of developments and prospects. *J. Magnes. Alloys* **2022**, *10*, 938–955. [[CrossRef](#)]
14. Zhang, B.; Zhang, W.; Zhang, F.; Ning, C.; An, M.; Yang, K.; Tan, L.; Zhang, Q. Degradable magnesium alloy suture promotes fibrocartilaginous interface regeneration in a rat rotator cuff transosseous repair model. *J. Magnes. Alloys* **2024**, *12*, 384–393. [[CrossRef](#)]
15. Liu, Z.; Cheng, X.; Peng, X.; Wang, P.; Zhao, X.; Liu, J.; Qu, R. A review of common-mode voltage suppression methods in wind power generation. *Renew. Sustain. Energy Rev.* **2024**, *203*, 114773. [[CrossRef](#)]
16. Wang, Z.; Deng, R.; Wang, Y.; Pan, F. Comparison of Construction Strategies of Solid Electrolyte Interface (SEI) in Li Battery and Mg Battery—A Review. *Molecules* **2024**, *29*, 4761. [[CrossRef](#)]
17. Yaghoubi, E.; Yaghoubi, E.; Khamees, A.; Razmi, D.; Lu, T. A systematic review and meta-analysis of machine learning, deep learning, and ensemble learning approaches in predicting EV charging behavior. *Eng. Appl. Artif. Intell.* **2024**, *135*, 108789. [[CrossRef](#)]
18. Poblan-Salas, C.A.; Henao, J.; Giraldo-Betancur, A.L.; Forero-Sossa, P.; Espinosa-Arbelaez, D.G.; González-Sánchez, J.A.; Dzib-Pérez, L.R.; Estrada-Moo, S.T.; Pech-Pech, I.E. HVOF-sprayed HA/S53P4 BG composite coatings on an AZ31 alloy for potential applications in temporary implants. *J. Magnes. Alloys* **2024**, *12*, 345–360. [[CrossRef](#)]
19. Hu, S.; Wang, Z.; Wang, J.; Pang, S.; Wang, B.; Zhu, M. An overview of silicon-air batteries: Principle, current state and future perspectives. *Coord. Chem. Rev.* **2024**, *517*, 216045. [[CrossRef](#)]
20. Xing, F.; Li, S.; Yin, D.; Xie, J.; Rommens, P.M.; Xiang, Z.; Liu, M.; Ritz, U. Recent progress in Mg-based alloys as a novel bioabsorbable biomaterials for orthopedic applications. *J. Magnes. Alloys* **2022**, *10*, 1428–1456. [[CrossRef](#)]
21. Saha, S.; Lestari, W.; Dini, C.; Sarian, M.N.; Hermawan, H.; Barão, V.A.; Sukotjo, C.; Takoudis, C. Corrosion in Mg-alloy biomedical implants- the strategies to reduce the impact of the corrosion inflammatory reaction and microbial activity. *J. Magnes. Alloys* **2022**, *10*, 3306–3326. [[CrossRef](#)]
22. Wang, G.; Yang, J.; Li, R. Imbalanced SVM-Based Anomaly Detection Algorithm for Imbalanced Training Datasets. *ETRI J.* **2017**, *39*, 621–631. [[CrossRef](#)]
23. Choudhary, L.; Banerjee, P.C.; Raman, R.S.; Lobo, D.E.; Easton, C.D.; Majumder, M.; Witte, F.; Löffler, J.F. Graphene–calcium carbonate coating to improve the degradation resistance and mechanical integrity of a biodegradable implant. *J. Magnes. Alloys* **2024**, *12*, 394–404. [[CrossRef](#)]
24. Bairagi, D.; Mandal, S. A comprehensive review on biocompatible Mg-based alloys as temporary orthopaedic implants: Current status, challenges, and future prospects. *J. Magnes. Alloys* **2022**, *10*, 627–669. [[CrossRef](#)]
25. Duan, Y.; Zhao, Y.; Hu, J. An initialization-free distributed algorithm for dynamic economic dispatch problems in microgrid: Modeling, optimization and analysis. *Sustain. Energy Grids Netw.* **2023**, *34*, 101004. [[CrossRef](#)]
26. Krüger, D.; Zeller-Plumhoff, B.; Wiese, B.; Yi, S.; Zuber, M.; Wieland, D.F.; Moosmann, J.; Willumeit-Römer, R. Assessing the microstructure and in vitro degradation behavior of Mg-xGd screw implants using µCT. *J. Magnes. Alloys* **2021**, *9*, 2207–2222. [[CrossRef](#)]
27. Chen, W.; Hou, H.; Zhang, Y.; Liu, W.; Zhao, Y. Thermal and solute diffusion in α -Mg dendrite growth of Mg-5wt.%Zn alloy: A phase-field study. *J. Mater. Res. Technol.* **2023**, *24*, 8401–8413. [[CrossRef](#)]
28. Tsakiris, V.; Tardei, C.; Clicinschi, F.M. Biodegradable Mg alloys for orthopedic implants—A review. *J. Magnes. Alloys* **2021**, *9*, 1884–1905. [[CrossRef](#)]

29. Zhang, J.; Feng, X.; Zhou, J.; Zang, J.; Wang, J.; Shi, G.; Li, Y. Series-Shunt Multiport Soft Normally Open Points. *IEEE Trans. Ind. Electron.* **2023**, *70*, 10811–10821. [[CrossRef](#)]
30. Farshid, S.; Kharaziha, M.; Atapour, M. A self-healing and bioactive coating based on duplex plasma electrolytic oxidation/polydopamine on AZ91 alloy for bone implants. *J. Magnes. Alloys* **2023**, *11*, 592–606. [[CrossRef](#)]
31. Zhao, W.; Ma, X.; Wang, X.; Zhou, H.; He, X.; Yao, Y.; Ren, Y.; Luo, Y.; Zheng, D.; Sun, S.; et al. Synergistically Coupling Atomic-Level Defect-Manipulation and Nanoscopic-Level Interfacial Engineering Enables Fast and Durable Sodium Storage. *Small* **2024**, *20*, e2311055. [[CrossRef](#)] [[PubMed](#)]
32. Gong, Y.; Wei, K.; Jiang, W.; Xiang, C.; Ding, H.; Wang, Z. Effect of Zn Addition on the Microstructure and Discharge Performance of Mg-Al-Mn-Ca Alloys for Magnesium-Air Batteries. *Metals* **2024**, *14*, 1014. [[CrossRef](#)]
33. Zhao, W.; Ma, X.; Wang, G.; Tan, L.; Wang, X.; He, X.; Wang, Y.; Luo, Y.; Zheng, D.; Sun, S.; et al. Significantly enhanced ion-migration and sodium-storage capability derived by strongly coupled dual interfacial engineering in heterogeneous bimetallic sulfides with densified carbon matrix. *SusMat* **2024**, *4*, e198. [[CrossRef](#)]
34. Oladapo, B.I.; Olawumi, M.A.; Omigbodun, F.T. Machine Learning for Optimising Renewable Energy and Grid Efficiency. *Atmosphere* **2024**, *15*, 1250. [[CrossRef](#)]
35. Liu, H.; Zhang, T.; Xu, J. Discharge Properties and Electrochemical Behaviors of Mg-Zn-xSr Magnesium Anodes for Mg–Air Batteries. *Materials* **2024**, *17*, 4179. [[CrossRef](#)]
36. Tolstopiatova, E.G.; Salnikova, Y.D.; Holze, R.; Kondratiev, V.V. Progress and Challenges of Vanadium Oxide Cathodes for Rechargeable Magnesium Batteries. *Molecules* **2024**, *29*, 3349. [[CrossRef](#)]
37. Yang, J.; Xu, W.; Ma, K.; Li, C. A Three-Stage Multi-Energy Trading Strategy Based on P2P Trading Mode. *IEEE Trans. Sustain. Energy* **2023**, *14*, 233–241. [[CrossRef](#)]
38. Yang, Z.; Zhou, S.; Zu, J.; Inman, D. High-Performance Piezoelectric Energy Harvesters and Their Applications. *Joule* **2018**, *2*, 642–697. [[CrossRef](#)]
39. Ma, K.; Yu, Y.; Yang, B.; Yang, J. Demand-Side Energy Management Considering Price Oscillations for Residential Building Heating and Ventilation Systems. *IEEE Trans. Ind. Inform.* **2019**, *15*, 4742–4752. [[CrossRef](#)]
40. Huang, J.; Wang, Y.; Guo, L. Energy intensity and energy-specific technological progress: A case study in Guangdong province of China. *Renew. Energy* **2022**, *184*, 990–1001. [[CrossRef](#)]
41. Wang, Z.; Wang, S.; Wang, X.; Luo, X. Permanent Magnet-Based Superficial Flow Velometer With Ultralow Output Drift. *IEEE Trans. Instrum. Meas.* **2023**, *72*, 1–12. [[CrossRef](#)]
42. Guigon, R.; Chaillout, J.J.; Jager, T.; Despesse, G. Harvesting raindrop energy: Experimental study. *Smart Mater. Struct.* **2008**, *17*, 015039. [[CrossRef](#)]
43. Li, S.; Zhou, J.; Zhou, F.; Niu, F.; Deng, W. A Reduced Current Ripple Overmodulation Strategy for Indirect Matrix Converter. *IEEE Trans. Ind. Electron.* **2024**, 1–10. [[CrossRef](#)]
44. Wang, R.; Liu, S.; Wang, L.; Li, Q.; Zhang, S.; Chen, B.; Jiang, L.; Zhang, Y. Superior energy-saving splitter in monoethanolamine-based biphasic solvents for CO₂ capture from coal-fired flue gas. *Appl. Energy* **2019**, *242*, 302–310. [[CrossRef](#)]
45. Liu, M.; Qian, F.; Mi, J.; Zuo, L. Dynamic interaction of energy-harvesting backpack and the human body to improve walking comfort. *Mech. Syst. Signal Process.* **2022**, *174*, 109101. [[CrossRef](#)]
46. Liu, F.; Zhao, X.; Zhu, Z.; Zhai, Z.; Liu, Y. Dual-microphone active noise cancellation paved with Doppler assimilation for TADS. *Mech. Syst. Signal Process.* **2023**, *184*, 109727. [[CrossRef](#)]
47. Riahi, K.; Van Vuuren, D.P.; Kriegler, E.; Edmonds, J.; O'Neill, B.C.; Fujimori, S.; Bauer, N.; Calvin, K.; Dellink, R.; Frick, O.; et al. The Shared Socioeconomic Pathways and their energy, land use, and greenhouse gas emissions implications: An overview. *Glob. Environ. Chang.* **2017**, *42*, 153–168. [[CrossRef](#)]
48. Sun, Q.; Lyu, G.; Liu, X.; Niu, F.; Gan, C. Virtual Current Compensation-Based Quasi-Sinusoidal-Wave Excitation Scheme for Switched Reluctance Motor Drives. *IEEE Trans. Ind. Electron.* **2024**, *71*, 10162–10172. [[CrossRef](#)]
49. Abbas, D.; Current, D.; Phillips, M.; Rossman, R.; Hoganson, H.; Brooks, K.N. Guidelines for harvesting forest biomass for energy: A synthesis of environmental considerations. *Biomass Bioenergy* **2011**, *35*, 4538–4546. [[CrossRef](#)]
50. Wang, S.; Wang, Z.; Dong, H.; Chen, Y. Recursive state estimation for stochastic non-linear non-Gaussian systems using energy-harvesting sensors: A quadratic estimation approach. *Automatica* **2023**, *147*, 110671. [[CrossRef](#)]
51. Meng, Q.; Tong, X.; Hussain, S.; Luo, F.; Zhou, F.; He, Y.; Liu, L.; Sun, B.; Li, B. Enhancing Distribution System Stability and Efficiency through Multi-Power Supply Startup Optimization for New Energy Integration. *IET Gener. Transm. Distrib.* **2024**, *early access*. [[CrossRef](#)]
52. Collier, S.H.C.; House, J.I.; Connor, P.M.; Harris, R. Distributed local energy: Assessing the determinants of domestic-scale solar photovoltaic uptake at the local level across England and Wales. *Renew. Sustain. Energy Rev.* **2023**, *171*, 113036. [[CrossRef](#)]
53. Viet, N.V.; Xie, X.D.; Liew, K.M.; Banthia, N.; Wang, Q. Energy harvesting from ocean waves by a floating energy harvester. *Energy* **2016**, *112*, 1219–1226. [[CrossRef](#)]
54. Beeby, S.P.; O'Donnell, T. Electromagnetic energy harvesting. In *Energy Harvesting Technologies*; Springer: Berlin/Heidelberg, Germany, 2009; pp. 129–161. [[CrossRef](#)]
55. Li, W.; Guo, X.; Zhang, Y.; Wang, K. A Comprehensive Review on the Synergetic Effect of Physicochemical Properties of Carbon Materials in Polysulfide Adsorption and Electrocatalysis for Advanced Li–S Batteries. *Chem. Eng. J.* **2023**, *459*, 141629. [[CrossRef](#)]

56. Guan, Z.; Li, P.; Wen, Y.; Du, Y.; Wang, Y. Efficient bubble energy harvesting by promoting pressure potential energy release using helix flow channel. *Appl. Energy* **2022**, *328*, 120159. [[CrossRef](#)]
57. Wang, W.; Cionca, V.; Wang, N.; Hayes, M.; O’Flynn, B.; O’Mathuna, C. Thermoelectric energy harvesting for building energy management wireless sensor networks. *Int. J. Distrib. Sens. Netw.* **2013**, *9*, 232438. [[CrossRef](#)]
58. Wang, Y.; Liu, X.; Tan, G.; Han, B.; Zhu, H.; Yuan, G. Electrocatalytic Water Splitting over Metal–Organic Framework-Derived Nanostructures. *Nano Res. Energy* **2022**, *1*, e9120015. [[CrossRef](#)]
59. Kassan, S.; Gaber, J.; Lorenz, P. Autonomous Energy Management System Achieving Piezoelectric Energy Harvesting in Wireless Sensors. *Mob. Netw. Appl.* **2020**, *25*, 794–805. [[CrossRef](#)]
60. Igliński, B.; Pietrzak, M.B.; Kiełkowska, U.; Skrzatek, M.; Kumar, G.; Piechota, G. The assessment of renewable energy in Poland on the background of the world renewable energy sector. *Energy* **2022**, *261*, 125319. [[CrossRef](#)]
61. Luo, R.; Yu, Z.; Wu, P.; Hou, Z. Analytical solutions of the energy harvesting potential from vehicle vertical vibration based on statistical energy conservation. *Energy* **2023**, *264*, 126111. [[CrossRef](#)]
62. Østergaard, P.A.; Duic, N.; Noorollahi, Y.; Mikulcic, H.; Kalogirou, S. Sustainable development using renewable energy technology. *Renew. Energy* **2020**, *146*, 2430–2437. [[CrossRef](#)]
63. Zhao, W.; Ma, X.; Gao, L.; Wang, X.; Luo, Y.; Wang, Y.; Li, T.; Ying, B.; Zheng, D.; Sun, S.; et al. Hierarchical Architecture Engineering of Branch-Leaf-Shaped Cobalt Phosphosulfide Quantum Dots: Enabling Multi-Dimensional Ion-Transport Channels for High-Efficiency Sodium Storage. *Adv. Mater.* **2024**, *36*, e2305190. [[CrossRef](#)] [[PubMed](#)]
64. Legerstee, W.J.; Kiriinya, L.; Kwakernaak, M.; Kelder, E.M. Magnesium Transfer between Atomic Force Microscopy Probes and Metal Electrodes in Aqueous Alginate Electrolytes. *Polymers* **2024**, *16*, 1615. [[CrossRef](#)] [[PubMed](#)]
65. Xia, J.; Liang, F.; Zhou, S.; Zhang, Y.; Wang, X.; Cao, J.; Cai, S.; Zhang, J.; Wang, L.; Zhu, Y.; et al. Recent Advances in Metal–Organic Frameworks and Their Derivatives for Electrocatalytic Water Splitting. *Chem. Eng. J.* **2022**, *433*, 134477. [[CrossRef](#)]
66. Li, C.; Liu, B.; Jiang, N.; Ding, Y. Elucidating the charge-transfer and Li-ion-migration mechanisms in commercial lithium-ion batteries with advanced electron microscopy. *Nano Res. Energy* **2022**, *1*, 9120031. [[CrossRef](#)]
67. Xu, Y.; Zhou, Y.; Li, Y.; Hao, Y.; Wu, P.; Ding, Z. Magnesium-Based Hydrogen Storage Alloys: Advances, Strategies, and Future Outlook for Clean Energy Applications. *Molecules* **2024**, *29*, 2525. [[CrossRef](#)]
68. Xie, X.D.; Wang, Q. Energy harvesting from a vehicle suspension system. *Energy* **2015**, *86*, 382–395. [[CrossRef](#)]
69. Zhang, H.; Li, P.; Jin, H.; Bi, R.; Xu, D. Non-linear wave energy dissipator with wave attenuation and energy harvesting at low frequencies. *Ocean. Eng.* **2022**, *266*, 112935. [[CrossRef](#)]

Disclaimer/Publisher’s Note: The statements, opinions and data contained in all publications are solely those of the individual author(s) and contributor(s) and not of MDPI and/or the editor(s). MDPI and/or the editor(s) disclaim responsibility for any injury to people or property resulting from any ideas, methods, instructions or products referred to in the content.